THE ASTROPHYSICAL JOURNAL, 457:291–320, 1996 January 20

A CONSISTENT METHOD OF CHARACTERISTICS FOR MULTIDIMENSIONAL MAGNETOHYDRODYNAMICS

DAVID A. CLARKE
Department of Astronomy and Physics, Saint Mary's University, Halifax, Canada NS B3H 3C3
Received 1995 March 13; accepted 1995 July 28

ABSTRACT

This paper introduces a previously unaddressed problem with performing multidimensional numerical MHD characterized by "explosive" growth (within a single time step) of weak magnetic fields to possibly dynamic strengths in the vicinity of strong velocity shear. This problem has been observed to occur in numerical algorithms which rely on the solution of the characteristic equations at the mesh interfaces. The solution to this problem is the subject of this paper and has led to an algorithm fundamentally different from those discussed previously. Specifically, at every point on the mesh, the magnetic induction terms are determined from the characteristic velocities which are evaluated by solving *implicitly* (in space) the characteristic equations for incompressible MHD (although the algorithm is perfectly suitable for compressible MHD). The implicit treatment of the characteristic equations sets this algorithm apart from previous efforts and is shown to be a necessary condition for multidimensional accuracy. It amounts to replacing the usual directional-split treatment of the induction and transport operators with a planar-split scheme.

Subject headings: MHD — methods: numerical

1. INTRODUCTION

Over the years, a variety of numerical algorithms for solving the equations of hydrodynamics have been developed and applied to numerous gas dynamical problems and, in particular, astrophysical systems. By no means is the following discussion an attempt to review all the efforts made in this area—such a review could itself be the subject of a full-length article. Instead, to set the stage for the present work, it is necessary to highlight only a handful of the numerical schemes developed for computational fluid and magnetofluid dynamics.

Arguably the most robust and efficient of the established hydrodynamical schemes is the class of Godunov and higher order Godunov algorithms developed over the past 35 years (e.g., Godunov 1959; van Leer 1979; Colella & Woodward 1984). A Godunov scheme is characterized by the exact solution to the Riemann problem at every mesh interface and at every time step. The piecewise parabolic method (PPM) of Colella & Woodward is an example of such a scheme and excels in its ability to perform *ideal* gasdynamics accurately with a minimum of mesh points. Schemes which may be described as "approximate Riemann solvers" include those reported by Roe (1981), Harten (1983), Harten et al. (1987), and others. These schemes retain many of the advantages of Godunov-type algorithms, yet are apparently more flexible in their ability to incorporate physics beyond ideal hydrodynamics. The family of flux-corrected transport (FCT) schemes originated by Boris & Book (1973) continue to be developed (e.g., Patnaik et al. 1987 and references therein) and are becoming competitive with higher order Godunov schemes such as PPM. Still a third class of numerical gasdynamics algorithms are the operator-split schemes stemming from the early work of J. R. Wilson and J. M. LeBlanc at the Lawrence Livermore National Laboratory. Recent applications of, and improvements on, these techniques are described by Norman & Winkler (1986) and Stone & Norman (1992a, hereafter SNa). Operator-split schemes use a variety of monotonic, upwinded, time-centered interpolation (MUTCI) algorithms on a staggered mesh. Although they can require several times the number of mesh points needed for a comparable Godunov scheme to resolve the same structures in three dimensions, they survive because they are much simpler to program, execute several times faster, and can be extended to include dissipative physics in a relatively straightforward manner.

Especially for astrophysical applications, it has become increasingly obvious that the consequences of magnetic fields cannot be ignored (e.g., Beck & Kronberg 1990; Kronberg 1994). Thus, various groups have extended existing hydrodynamical algorithms to include the effects of magnetic fields. Brio & Wu (1988) have developed an MHD algorithm based on Roe's scheme (1981); DeVore (1991) has developed an MHD extension for FCT; Zachary & Colella (1992) base their MHD algorithm on the scheme reported by Bell, Colella, & Trangenstein (1989); Dai & Woodward (1994) have developed a PPM MHD algorithm; Ryu & Jones (1995, hereafter RJ) report an MHD scheme based on Harten (1983), and so it goes. Meanwhile, numerous attempts have been made to incorporate magnetic fields into operator-split schemes, the most notable for the present work are those described by Evans & Hawley (1988, hereafter EH) and Stone & Norman (1992b, hereafter SNb).

Some notable applications of multidimensional MHD algorithms include, for example, the discovery of a powerful instability in rotating accretion disks (Balbus & Hawley 1992 and references therein). However, for the most part, multidimensional MHD applications to astrophysical phenomena have been limited. Indeed, this paper will show that even the best of the existing operator-split MHD algorithms (SNb) is prone to numerical "instabilities" of an "explosive" nature,[1] which appear rarely in

[1] The expression "instability" is used somewhat loosely in this context. Strictly speaking, numericists regard an algorithm as *unstable* only if it fails some well-defined test such as the von Neumann stability analysis (e.g., Richtmyer & Morton 1967), and such analyses do not uncover the effects reported in this paper. Instead, the "instabilities" discussed herein are perhaps better described as *significant errors* (i.e., signal-to-noise ratio of order unity or less) generated suddenly (within a single time step) by the numerical algorithm. For brevity and lack of better language, these will be referred to as "explosive instabilities."

two-dimensional and frequently in three-dimensional applications. As discussed below, the algorithmic solution to these numerical problems has led to a "planar-split" approach, rather than the traditional "directional-split" approach which is used by virtually all existing algorithms. The planar-split technique sets this scheme apart from other efforts, such as those listed above, and may be an approach beneficial to Godunov-type, Godunov-like, and FCT schemes as well.

The equations of ideal MHD as discussed in this paper are

$$\frac{\partial \rho}{\partial t} + \nabla \cdot (\rho \boldsymbol{v}) = 0 , \tag{1}$$

$$\frac{\partial \boldsymbol{s}}{\partial t} + \nabla \cdot (\boldsymbol{s}\boldsymbol{v}) = -\nabla p + (\nabla \times \boldsymbol{B}) \times \boldsymbol{B} = -\nabla\left(p + \frac{B^2}{2}\right) + (\boldsymbol{B} \cdot \nabla)\boldsymbol{B} , \tag{2}$$

$$\frac{\partial e}{\partial t} + \nabla \cdot (e\boldsymbol{v}) = -p\nabla \cdot \boldsymbol{v} , \tag{3}$$

$$\frac{\partial \boldsymbol{B}}{\partial t} = \nabla \times (\boldsymbol{v} \times \boldsymbol{B}) , \tag{4}$$

where the system of four equations in six variables (ρ—matter density, $\boldsymbol{v}$—flow velocity, $\boldsymbol{s}$—momentum per unit volume, p—thermal pressure, $\boldsymbol{B}$—magnetic induction, and e—thermal energy density per unit volume) are closed by the following relations:

$$\boldsymbol{s} = \rho \boldsymbol{v} , \tag{5}$$

$$p = p(\rho, e) \qquad \text{(equation of state)} . \tag{6}$$

Alternatively, one may replace equation (3) with a "total energy equation," which describes the time evolution of the combined internal, kinetic, and magnetic energy densities. This variation has its advantages and disadvantages over solving equation (3) and is discussed further in Appendix B.

In this paper, $\boldsymbol{B}$ is expressed in the somewhat nontraditional units in which the magnetic pressure (p_B) and the Alfvén velocity ($\boldsymbol{a}$) are given by

$$p_B = B^2/2 , \tag{7}$$

$$\boldsymbol{a} = \frac{\boldsymbol{B}}{\sqrt{\rho}} . \tag{8}$$

In other words, the permeability of free space (μ_0 in mks) is set to 1.

The left-hand sides of equations (1), (2), and (3) each have the form $(\partial/\partial t + \nabla \cdot \boldsymbol{v})q$, where $q = \rho$, $\boldsymbol{s}$, or e. This form is sometimes described as "volume-conservative" and is useful numerically because, when differenced, the volume integral over a mesh zone of the variable q is conserved numerically to within machine round-off errors. For example, the volume integral of ρ is the total mass in the mesh zone whose exact conservation is clearly a desired virtue of any acceptable numerical scheme.

In contrast, equation (4) is not and should not be written in volume-conservative form, because the conserved quantity associated with the magnetic field is the surface integral of $\boldsymbol{B}$ over each mesh element (i.e., the magnetic flux $\Phi_B = \int \boldsymbol{B} \cdot d\boldsymbol{A}$) and not the volume integral. While it is possible to force equation (4) into volume-conservative form (presumably so the numerical techniques developed for eqs. [1], [2], and [3] may be used), this approach is ill advised since it will necessarily introduce terms on both sides of the equality which may cancel exactly analytically, but will only cancel to within the numerical truncation error of the differenced induction equation. These truncation errors could be severe in the vicinity of steep gradients, introducing nonphysical effects (e.g., magnetic monopoles) into the solution because the true conserved quantity (namely, Φ_B) will not be conserved to within machine round-off errors.

Instead, equation (4) as it is written *is* the desired form (e.g., "surface-conservative" form) since the right-hand side is a perfect curl. Thus, the divergence of the right-hand side of equation (4) will be zero analytically (by definition) and numerically (by construct). This ensures strict conservation of magnetic flux or, equivalently, preserves $\nabla \cdot \boldsymbol{B} = 0$ everywhere to within machine round-off errors. This is the crux of the argument in EH, which led to the development of the constrained transport (CT) algorithm for updating magnetic fields (reviewed in § 3.1).

An overview of the rest of the paper is as follows: Section 2 introduces the nomenclature used throughout the paper and details the groundwork of an operator-split MHD algorithm. Section 3 outlines the consistent method of characteristics (CMoC), designed to transport momenta and perform magnetic induction simultaneously and stably in multidimensions. Section 4 describes various problems to demonstrate the CMoC algorithm. Finally, § 5 discusses other aspects of the algorithm and presents some preliminary results from a three-dimensional computation in progress. Additional details are relegated to the appendices.

2. GROUNDWORK

To cast the continuous differential equations (1)–(4) into a form tractable to a numerical algorithm, one first integrates equations (1), (2), and (3) over the zone volume, and equation (4) over the zone surface area, so conserved quantities are considered exclusively.

Thus,

$$\frac{d}{dt}\int_V \rho\, dV + \oint_A \rho(v - v_g)\cdot dA = 0\,, \tag{9}$$

$$\frac{d}{dt}\int_V s\, dV + \oint_A s(v - v_g)\cdot dA = -\oint_A \left(p + \frac{B^2}{2}\right) dA + \int_V (B\cdot\nabla)B\, dV\,, \tag{10}$$

$$\frac{d}{dt}\int_V e\, dV + \oint_A e(v - v_g)\cdot dA = -\int_V p\nabla\cdot v\, dV\,, \tag{11}$$

$$\frac{d}{dt}\int_A B\cdot dA - \oint_l [(v - v_g)\times B]\cdot dl = 0\,, \tag{12}$$

where integrations are performed over zone volumes (V), surface areas (A), or face perimeters (l), and where v_g is a grid velocity relative to an Eulerian observer introduced in the case of an adaptive mesh. Henceforth, v_g will be set to zero. Differentials in equations (9)–(12) are replaced with finite differences to yield the *difference* form of the MHD equations.

In an operator-split algorithm, the variables are updated in two distinct steps, namely, the *source* step and the *transport* step. In the source step, the variables s and e are updated with the terms on the right-hand side of equations (10) and (11). Other "source terms" deemed necessary to broaden the physics (e.g., gravity, dissipation, etc.) can be incorporated into this step. The transport step, in which the fluxes of the variables are transported across zone boundaries, consists of the closed integrals ($\oint$) on the left-hand sides of equations (9)–(12) and completes the update of the variables for each time step.

In a three-dimensional staggered grid, there are two sets of grid vectors, and, in this paper, they are defined thus. Consider the (i, j, k)th zone in a three-dimensional mesh (Fig. 1). The "a-grid," namely, $(x_{1a}(i), x_{2a}(j), x_{3a}(k))$, are the coordinates of the corner of the zone closest to zone (1, 1, 1) (point "A" in Fig. 1). The "b-grid," namely, $(x_{1b}(i), x_{2b}(j), x_{3b}(k))$, are the coordinates of the zone center (point "B" in Fig. 1). The names used for the coordinates, namely, (x_{1c}, x_{2c}, x_{3c}), $c = a, b$, are intentionally generic and may be thought of as (x, y, z) in Cartesian coordinates, (z, r, ϕ) in cylindrical coordinates, and (r, θ, ϕ) in spherical polar coordinates. Differences among these coordinate systems can be relegated to well-defined metric terms (SNa), which are then retained in the difference equations. For simplicity of notation, this work shall be restricted to Cartesian geometry, though extension to cylindrical and spherical polar coordinates is straightforward.

In a staggered grid, the scalar variables (ρ, e) are "zone-centered," while the vector variables (v, B) are "face-centered" (Fig. 1). Indeed, much of the accuracy and robustness of the algorithm described herein can be attributed directly to the staggered nature of the grid. Within this framework, spatial differences of variables are located halfway between the differenced values. Thus, gradient components of zone-centered scalars are face-centered quantities, divergences of face-centered vectors are zone-centered, and curl components of face-centered vectors (e.g., the current density $J = \nabla \times B$) are "edge-centered." Note, too, that grid variables have specific locations attributed to them. Thus, $x_{1a}(i)$ is a face-centered quantity while $dx_{1a}(i) = x_{1a}(i + 1) - x_{1a}(i)$ is a zone-centered quantity. Similarly, $x_{1b}(i)$ is a zone-centered quantity, while $dx_{1b}(i) = x_{1b}(i) - x_{1b}(i - 1)$ is a face-centered quantity.

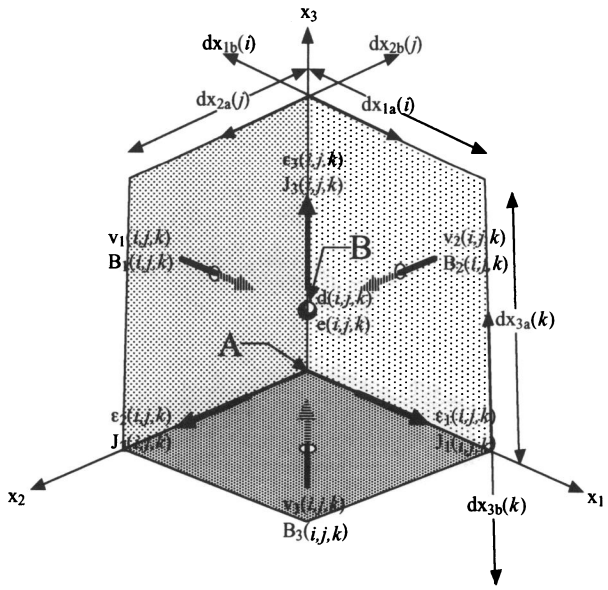

FIG. 1.—Depiction of a single three-dimensional Cartesian zone showing the location of the various flow variables. The primary scalars (ρ, e) are zone-centered (point "B"), while the primary vectors (v, B) are face-centered and point toward the zone center. Derived vectors (e.g., the emf's and the current density J) are edge-centered, lying along the edges of the zones. The corner labeled "A" is the (i, j, k)th corner and is the nearest corner to the observer.

Equations (9)–(12) can now be differenced directly. All difference equations appearing in this paper use the following nomenclature. The indices (i, j, k) indicate the variable value at the (i, j, k)th zone located at the zone center, zone face, or zone edge as discussed above. The superscript n denotes the nth time step, while the superscripts S and T_m indicate the variable has been updated for source terms and transport in the m-direction, $m = 1$, 2, and 3, respectively. Note that in this scheme the set of superscripts (n, S, T_1, T_2, T_3) is equivalent to the superscript $(n + 1)$. Finally, the *continuous* variables $(\rho, e, p, \boldsymbol{v}, \boldsymbol{B})$ [functions of time and space $(t, \boldsymbol{r})$] appearing in equations (9)–(12) correspond in the remainder of the paper to the *discrete* variables $(d, e, p, v_1, v_2, v_3, B_1, B_2$, and $B_3)$, respectively [now functions of the discrete grid (n, i, j, k)] in the differenced equations.

2.1. *Time-Step Determination*

The time step for an explicit algorithm such as this is determined by the "CFL condition" (Courant, Friedrichs, & Lewy 1928; Richtmyer & Morton 1967) which stems from a von Neumann stability analysis. Physically, one can interpret the CFL condition to mean no signal shall cross more than one mesh zone in any given time step. This, in turn, may be interpreted in terms of causality: each zone must "know" about each wave passing through it if the wave is to have any effect on it. Numerically, violation of the CFL condition in an explicit scheme may induce numerical instabilities whose nature could grow to dominate the flow (e.g., Richtmyer & Morton 1967). Conversely, implicit schemes are designed to remain stable for arbitrarily large time steps (e.g., Richtmyer & Morton 1967 for a general overview). While implicit schemes are, in principle, useful for systems which possess unmanageably short timescales (e.g., radiation hydrodynamics—Stone, Mihalas, & Norman 1992), one may still be forced to choose time steps comparable to the CFL condition limit if all waveforms are to be propagated accurately.

In this work, the nth time step is given by

$$(dt^n)^{-2} = \mathscr{C}^{-2} \underset{\forall i,j,k}{\mathrm{MAX}} \left[\frac{[c(i,j,k)]^2 + [a(i,j,k)]^2}{\mathrm{MIN}\,\{[dx_{1a}(i)]^2, [dx_{2a}(j)]^2, [dx_{3a}(k)]^2\}} + \left[\frac{v_1^n(i,j,k)}{dx_{1a}(i)}\right]^2 + \left[\frac{v_2^n(i,j,k)}{dx_{2a}(j)}\right]^2 + \left[\frac{v_3^n(i,j,k)}{dx_{3a}(k)}\right]^2 \right], \quad (13)$$

where $\mathscr{C} < 1$ is the "Courant number" typically chosen between 0.5 and 0.9, and where $c(i, j, k)$ and $a(i, j, k)$ are the local sound and Alfvén speeds, respectively given by

$$c(i,j,k)^2 = \frac{\gamma p^n(i,j,k)}{d^n(i,j,k)}, \quad (14)$$

$$a(i,j,k)^2 = \frac{1}{4d^n(i,j,k)} \{[B_1^n(i,j,k) + B_1^n(i+1,j,k)]^2 + [B_2^n(i,j,k) + B_2^n(i,j+1,k)]^2 + [B_3^n(i,j,k) + B_3^n(i,j,k+1)]^2\}, \quad (15)$$

where γ is the adiabatic index of the ideal gas, $p^n(i, j, k)$ and $d^n(i, j, k)$ are the numerical values of the (zone-centered) pressure and density, respectively, and $v_a^n(i, j, k)$ and $B_a^n(i, j, k)$, $a = 1$, 2, 3, are the numerical values of the 1-, 2-, and 3-components of the (face-centered) velocity and magnetic field, respectively, all at time step n and at the (i, j, k)th zone.

Strictly speaking, the square of the fast wave speed might be used in determining the time step in equation (13) instead of $c^2 + a^2$. The latter, however, is an acceptable upper limit to the former.

In principle, since artificial viscosity is used to stabilize shocks, the dissipative timescale should be incorporated into the time-step selection. In practice, the viscous time step for supersonic flow with moderately strong shocks can be several times smaller than the CFL condition as given by equation (13), thus requiring several times the number of time steps an algorithm without artificial viscosity (such as PPM) would need. This effect can eliminate much of the advantage in computational speed an operator-split algorithm might have over PPM. Fortunately, this problem can be circumvented by "subcycling" on the dissipative timescales (discussed in Appendix A) thereby obviating the need to use smaller time steps than that prescribed by equation (13).

Finally, increases in the time step are limited to 25% per cycle to maintain accuracy in the event of radical dynamical changes, while decreases are unrestricted to ensure numerical stability (e.g., Norman & Winkler 1986).

2.2. *Source Step*

The difference form for the source terms in the 1-component of equation (10) is

$$s_1^{n,S}(i,j,k) = s_1^n(i,j,k) - dt^n \frac{p_T^n(i,j,k) - p_T^n(i-1,j,k)}{dx_{1b}(i)}, \quad (16)$$

where the momentum (s_1) is given by:

$$s_1^n(i,j,k) = \frac{d^n(i,j,k) + d^n(i-1,j,k)}{2} v_1^n(i,j,k), \quad (17)$$

and where

$$p_T^n(i,j,k) = (\gamma - 1)e^n(i,j,k) + \tfrac{1}{4}\{[B_2^n(i,j,k)]^2 + [B_2^n(i,j+1,k)]^2 + [B_3^n(i,j,k)]^2 + [B_3^n(i,j,k+1)]^2\}. \quad (18)$$

Note that p_T^n is a "total" pressure, consisting of the thermal pressure plus a suitable spatial average of the effect of compressing the magnetic field in the 1-direction (area integral on the right-hand side of eq. [10] without the B_1^2 term). Source terms arising from the shear of the magnetic field (volume integral on the right-hand side of eq. [10] with the B_1^2 term from the area integral) are accounted for during the combined induction and momentum transport step (§ 3.3). Other forces such as gravity and "fictitious forces" arising from a curvilinear coordinate system would be applied here as well (see SNa). Source terms arising from artificial

viscous stresses are discussed in Appendix A. The difference form for the source terms for the 2- and 3-components of equation (10) are obtained by permuting all labels ($1 \rightarrow 2 \rightarrow 3 \rightarrow 1$) and indices ($i \rightarrow j \rightarrow k \rightarrow i$) in equations (16), (17), and (18).

After the source terms (forces) have been applied to the momenta, the velocities are updated in the obvious way, namely,

$$v_1{}^{n,S}(i, j, k) = \frac{2}{d^n(i, j, k) + d^n(i-1, j, k)}\, s_1{}^{n,S}(i, j, k) . \tag{19}$$

The source terms for the internal energy density are applied *after* the velocity and viscous (Appendix A) updates. The difference form for the internal energy source terms (eq. [11]) is

$$e^{n,S}(i, j, k) = \frac{1-\zeta}{1+\zeta}\, e^n(i, j, k) , \qquad p\,dV \text{ term} , \tag{20}$$

where

$$\zeta \equiv \frac{\gamma - 1}{2}\, dt^n \left[\frac{v_1{}^{n,S}(i+1, j, k) - v_1{}^{n,S}(i, j, k)}{dx_{1a}(i)} + \frac{v_2{}^{n,S}(i, j+1, k) - v_2{}^{n,S}(i, j, k)}{dx_{2a}(j)} + \frac{v_3{}^{n,S}(i, j, k+1) - v_3{}^{n,S}(i, j, k)}{dx_{3a}(k)} \right] . \tag{21}$$

Because of the staggered grid, all terms in the velocity divergence are cospatial at the zone center with the internal energy density variable e^n. Note that the energy source term has been applied implicitly. Performing this step explicitly requires no less effort and can result in obvious problems in the vicinity of steep gradients such as shocks. Source terms arising from artificial viscous heating are discussed in Appendix A.

2.3. *Scalar Transport Step*

The "transport step" accounts for the fluid motions across grid boundaries and is where operator-split algorithms are most prone to numerical instabilities and inaccuracies. Accordingly, the majority of development for such schemes has been focused on how to perform the transport step accurately and stably. To date, operator-split MHD algorithms have been designed with the transport and induction steps decoupled (e.g., EH and SNb). However, in § 3, the case is made that the momentum transport and magnetic field induction steps are fundamentally linked and should be accounted for simultaneously. Thus, discussion shall be limited here to the transport of the zone-centered scalars only. Momentum transport will be deferred to the discussion surrounding the numerical induction of magnetic field.

Let $q^n(i, j, k)$ be either the density (d^n, mks units: kg m^{-3}) or the internal energy density (e^n, mks units: J m^{-3}). Then, transport of q^n across the 1-interface is given by differencing the area integrals in equations (9) and (11):

$$q^{n,S,T_1}(i, j, k) = q^{n,S}(i, j, k) - \frac{\mathscr{F}_1(i+1, j, k) - \mathscr{F}_1(i, j, k)}{dx_{1a}(i)} , \tag{22}$$

where $\mathscr{F}_1(i, j, k)$ (located at the i-face center) is an estimate of the flux of $q^{n,S}$ crossing the i-face and is given by

$$\mathscr{F}_1(i, j, k) \equiv \mathscr{M}_1(i, j, k)\overline{[q^{n,S}(i, j, k)/d^n(i, j, k)]}^{\,i} , \tag{23}$$

where the mass flux across the i-face [$\mathscr{M}_1(i, j, k)$] is given by

$$\mathscr{M}_1(i, j, k) \equiv \overline{d^n(i, j, k)}^{\,i}\, v_1{}^{n,S}(i, j, k)\, dt^n , \tag{24}$$

and where the "$\overline{}^{\,i}$" construct indicates the variable or quotient of variables is *interpolated* to the i-face. Various forms of interpolation are possible so long as they abide by three fundamental requirements for stability and accuracy:

1. Interpolation must be monotonic (introduce no extrema at the interpolation site).
2. Interpolation must be upwinded (determined from the upwinded side of the interface) and preserve "positivity" (amount transported from a given zone must always be less than the zone contents).
3. Interpolation must be time-centered (to reduce diffusion and preserve the accuracy of the interpolation scheme).

A number of monotonic, upwinded, time-centered interpolation (MUTCI) schemes have been devised and may be used depending upon the relative importance of accuracy and computational speed. A first-order "donor cell" prescription (interpolation in the i-direction) is given by

$$\overline{q^{n,S}(i, j, k)}^{\,i} = \begin{cases} q^{n,S}(i-1, j, k) & (\xi \geq 0) , \\ q^{n,S}(i, j, k) & (\xi < 0) , \end{cases} \tag{25}$$

where $\xi \equiv v_1{}^{n,S}(i, j, k)\, dt^n$. A second-order MUTCI scheme first suggested by van Leer (1977) is given by

$$\overline{q^{n,S}(i, j, k)}^{\,i} = \begin{cases} q^{n,S}(i-1, j, k) + \delta q(i-1, j, k)\left[1 - \dfrac{\xi}{dx_{1a}(i-1)}\right] & (\xi \geq 0) , \\ q^{n,S}(i, j, k) - \delta q(i, j, k)\left[1 + \dfrac{\xi}{dx_{1a}(i)}\right] & (\xi < 0) , \end{cases} \tag{26}$$

where

$$\delta q(i, j, k) = \begin{cases} \dfrac{dq(i+1, j, k)\, dq(i, j, k)}{dq(i+1, j, k) + dq(i, j, k)} & [dq(i+1, j, k)\, dq(i, j, k) > 0] , \\ 0 & (\text{otherwise}) , \end{cases} \tag{27}$$

$$dq(i, j, k) \equiv q^{n,S}(i, j, k) - q^{n,S}(i-1, j, k) . \tag{28}$$

In equation (26), the dependence on the sign of the velocity (i.e., ξ) provides upwindedness while the dependence on dt^n time-centers the interpolation. Equation (27) ensures monotonicity and positivity. Note that contrary to claims made in SNa, this form of the van Leer (1977) interpolation scheme is *fully* general for both uniform and nonuniform grids. The generalization suggested in SNa actually *removes* the effect of a nonuniform grid and can violate positivity under certain circumstances.

Finally, a robust third-order MUTCI scheme is given by Colella & Woodward (1984). It is too complicated to reproduce here, and the interested reader is referred to their lucid description. Comparisons of all three MUTCI schemes may be found in SNa.

The details of the transport step as embodied by equations (22), (23), and (24) encompass the idea of "consistent advection" first introduced by Norman, Wilson, & Barton (1980). Consistent advection was invented to circumvent the problem of angular momentum diffusion in accretion disks, but has implications even in simple one-dimensional Cartesian advection test problems. Consistent advection imposes the additional constraint that all the variables will be transported in a way *consistent* with the transport of matter. Without this constraint, numerical truncation errors may result in matter and momentum transport occurring (locally) in opposite directions, contrary to physical reason.

In a consistent advection scheme, one first defines the mass fluxes across every interface (eq. [24]) and then constructs the fluxes of the variable $q^{n,S}$ by multiplying the mass flux with a MUTCI of the ratio $q^{n,S}/d^n$ (eq. [23]). Thus, for the density itself, the mass fluxes are already the appropriate fluxes to use. Internal energy density fluxes are formed by multiplying the mass fluxes by the MUTCI of the *specific* energy density (proportional to temperature). Finally, momentum fluxes could be constructed by multiplying the mass fluxes by the MUTCI of the velocity (e.g., SNa), although, as seen in § 3.3, it is better to multiply the mass fluxes by the CMoC estimate of the velocity instead.

The reader should be reminded at this point that the above discussion specifically assumes a Cartesian coordinate system. The generalization to a curvilinear system such as cylindrical or spherical polar coordinates is cumbersome, though straightforward, and requires the use of metric terms, zone volumes, and areas of zone faces which depend upon the coordinate values. The interested reader is referred to SNa for a well-developed example of a fully "covariant" treatment of the difference equations.

Finally, difference expressions for the transport of scalars in the 2- and 3-directions are given by

$$q^{n,S,T_1,T_2}(i, j, k) = q^{n,S,T_1}(i, j, k) - \frac{\mathscr{F}_2(i, j+1, k) - \mathscr{F}_2(i, j, k)}{dx_{2a}(j)} , \tag{29}$$

$$q^{n,S,T_1,T_2,T_3}(i, j, k) \equiv q^{n+1}(i, j, k) = q^{n,S,T_1,T_2}(i, j, k) - \frac{\mathscr{F}_3(i, j, k+1) - \mathscr{F}_3(i, j, k)}{dx_{3a}(k)} , \tag{30}$$

where

$$\mathscr{F}_2(i, j, k) \equiv \mathscr{M}_2(i, j, k)\overline{[q^{n,S,T_1}(i, j, k)/d^{n,T_1}(i, j, k)]}^{j} , \tag{31}$$

$$\mathscr{F}_3(i, j, k) \equiv \mathscr{M}_3(i, j, k)\overline{[q^{n,S,T_1,T_2}(i, j, k)/d^{n,T_1,T_2}(i, j, k)]}^{k} , \tag{32}$$

and where

$$\mathscr{M}_2(i, j, k) \equiv \overline{d^{n,T_1}(i, j, k)}^{j} v_2^{n,S}(i, j, k)\, dt^n , \tag{33}$$

$$\mathscr{M}_3(i, j, k) \equiv \overline{d^{n,T_1,T_2}(i, j, k)}^{k} v_3^{n,S}(i, j, k)\, dt^n . \tag{34}$$

Expressions for the MUTCI of q^n in the 2- and 3-directions are given by permuting all labels and indices in equations (25)–(28). Note, in this manner of directional-splitting the transport operator, each direction is not treated symmetrically since the fluxes are determined from partially updated variables (e.g., eqs. [31] and [32]). Nevertheless, as a matter of practicality, this is the desired prescription, because it avoids carrying both the old data and the partially updated data simultaneously. It should be noted that there is no evidence to suggest using exclusively old values for all fluxes gives better or poorer accuracy than using partially updated values for the fluxes, nor is there any evidence to suggest permuting the order in which the partial updates are performed improves accuracy in general applications (J. Hawley 1990, private communication). However, for some test problems in which symmetric behavior is part of what is being tested (spherically symmetric explosions, for example), permuting the order of the partial updates can improve the symmetric appearance of the numerical solution. Therefore, performing such permutations may be a desirable attribute of a directional-split scheme.

It is clear there are a variety of ways to directional-split the scalar transport operator. The method presented here has proved to be robust, stable, accurate, and efficient, with both computational memory and speed.

3. MAGNETIC INDUCTION AND MOMENTUM TRANSPORT

To date, operator-split MHD schemes have treated momentum transport and magnetic induction independently. While simpler algorithmically, this approach is flawed from the outset, since it decouples the velocity and magnetic vector fields more than numerical accuracy would seem to permit. In this section, a scheme in which momentum transport and magnetic induction are

performed simultaneously (the CMoC) is detailed. In part, the CMoC is a logical extension of two other schemes which perform magnetic induction exclusively, namely, CT and the Method of Characteristics (MoC). Therefore, the role of these schemes as predecessors to the CMoC is included in the discussion below.

3.1. *Constrained Transport*

CT (EH) is a numerical scheme designed to solve the induction equation (eqs. [4] and [12]) while preserving $\nabla \cdot \boldsymbol{B} = 0$ to within machine round-off errors. Unlike methods which use the vector potential to evolve the magnetic field (e.g., Clarke, Norman, & Burns 1989), CT generalizes trivially to three dimensions, is simpler algorithmically, and produces more accurate results. Consider the magnetic flux penetrating the (i, j, k)th 1-interface (Fig. 2). Integrating equation (12) over the surface area of this interface (area S_1, normal $\boldsymbol{n}_1$) yields

$$\frac{d}{dt}\int_{\delta S_1} \boldsymbol{B}\cdot\boldsymbol{n}_1\, dS \equiv \frac{d\Phi_1}{dt} = \int_{\delta S_1} (\nabla \times \boldsymbol{\epsilon})\cdot \boldsymbol{n}_1\, dS = \oint_{\delta l} \boldsymbol{\epsilon}\cdot d\boldsymbol{l}\,, \tag{35}$$

where $\boldsymbol{\epsilon} = \boldsymbol{v} \times \boldsymbol{B}$ is the *emf* driving the evolution of the magnetic field. Differencing equation (35) in a manner consistent with Figure 2, one gets

$$(B_1\,\delta S_1)\big|^{n+1}_{i,j,k} = (B_1\,\delta S_1)\big|^{n}_{i,j,k} + dt^n\{[(\epsilon_3\,\delta l_3)\big|^{n}_{i,j+1,k} - (\epsilon_3\,\delta l_3)\big|^{n}_{i,j,k}] - [(\epsilon_2\,\delta l_2)\big|^{n}_{i,j,k+1} - (\epsilon_2\,\delta l_2)\big|^{n}_{i,j,k}]\}\,, \tag{36}$$

where, for Cartesian coordinates, the surface area is given by $\delta S_1(i, j, k) = \delta x_{2a}(j)\,\delta x_{3a}(k)$, and the edge lengths are given by $\delta l_2(i, j, k) = \delta x_{2a}(j)$ and $\delta l_3(i, j, k) = \delta x_{3a}(k)$. For a general coordinate system, δS_1, δl_2, and δl_3 are all functions of the metric as well as the coordinate differentials (SNa). The differenced form of the induction equation for the 2- and 3-components of the magnetic field may be determined from equation (36) by permuting the labels ($1 \to 2 \to 3 \to 1$) and indices ($i \to j \to k \to i$) cyclically. It is left as an exercise to show the induction equation so differenced will yield:

$$\frac{d}{dt}(\nabla \cdot \boldsymbol{B}) = 0 \tag{37}$$

to within machine round-off errors (EH). Thus, this scheme *preserves* the initial magnetic field divergence rather than guaranteeing it to be zero. It is therefore left to the user to ensure the magnetic divergence is *initialized* to zero.

Note that for face-centered magnetic field components, equation (36) requires the emf components to be "edge-centered" (as indicated in Fig. 2). It is also possible, however, to devise a scheme in which the magnetic field components themselves are edge-centered. In this case, the *emf*'s (and the current density) are face-centered quantities and thus cospatial with the velocity. With hindsight, this arrangement is excluded on the grounds that it treats the magnetic field and velocity asymmetrically when determining the *emf*'s and, thus, is inconsistent with both the MoC and CMoC algorithms.

Within CT, there exists an important degree of freedom: one may specify *any* prescription for the *emf* and maintain zero divergence in the magnetic field. Of course, the trick is to choose the best prescription for the *emf* which preserves both stability and accuracy. In the original CT scheme (EH), the prescription for estimating $\epsilon_3 = v_1 B_2 - v_2 B_1$ at the 3-edge, for example, is as follows:

$$\epsilon_3 = \langle v_1\rangle_2 \overline{B_2}^{\,1} - \langle v_2\rangle_1 \overline{B_1}^{\,2}\,, \tag{38}$$

where $\langle v_a\rangle_b$ is the 2-point average of v_a ($a = 1, 2$) in the b-direction ($b = 3 - a$), and, as before, $\overline{B_b}^{\,a}$ is the MUTCI of B_b in the a-direction, upwinded in velocity v_a. This scheme works well for advection problems (v = constant, $\boldsymbol{J} \times \boldsymbol{B} = 0$) but not so well for simple dynamical problems such as the propagation of a one-dimensional shear Alfvén wave. Consider the one-dimensional test

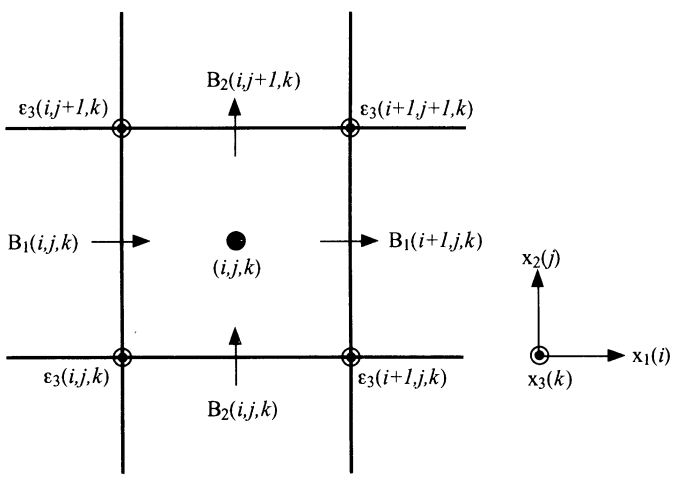

FIG. 2.—Two-dimensional slice through a zone (3-direction is normal to the page) showing the fundamentals of the CT algorithm. The magnetic field components are face-centered, while ϵ_3 is centered on the 3-edge. In this projection, ϵ_1 (ϵ_2) would be represented by arrows perpendicular to the B_2's (B_1's). Note that a 1-gradient in ϵ_3 generates B_2 and a 2-gradient in ϵ_3 generates B_1.

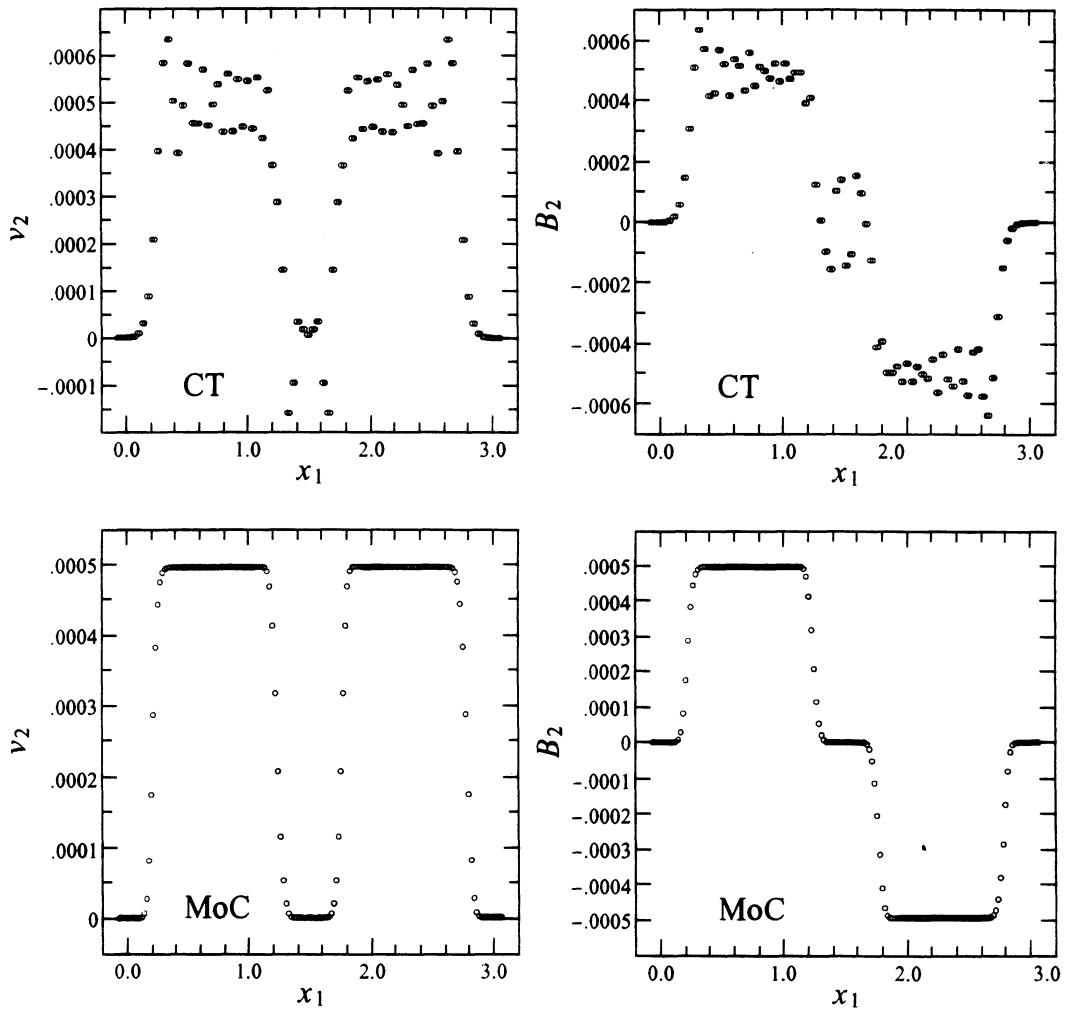

FIG. 3.—Two numerical attempts at propagating an Alfvén wave in one-dimension in which two square pulses in velocity (*left*) and magnetic field (*right*) are supposed to travel in opposite directions. Top two panels are the CT solution, while the bottom two are the MoC solution.

problem shown in Figure 3 performed with 150 uniform zones. A uniform density (1.0), internal energy (1.0), 1-velocity (0.0), and 1–magnetic field (1.0) are initialized across the entire grid, while the 2-velocity is set to 0.001 in the middle 50 zones only. In the remainder of the grid, the 2-velocity is set to 0.0. The excited Alfvén waves are allowed to propagate for $\frac{3}{4}$ of a pulse width with the results recorded in Figure 3. The top panels show the profiles of the 2-velocity and 2–magnetic field using the CT scheme. The lower two panels show the results using the MoC described in the next subsection. Since Alfvén waves are fundamental to any MHD system in which the magnetic field plays a dynamic role, the CT scheme for assigning the *emf* (eq. [38]) is clearly unsuitable for a general MHD scheme.

3.2. *The Method of Characteristics*

Let us continue to restrict the discussion to the evaluation of the 3-component of the *emf* (ϵ_3). At the end of § 3.3, the discussion is generalized to include ϵ_2 and ϵ_1. The MoC (SNb) evaluates ϵ_3 using the characteristics of incompressible MHD flow. Thus,

$$\epsilon_3 = v_1^* B_2^* - v_2^* B_1^* , \tag{39}$$

where the "starred" values are evaluated from values of v_1, v_2, B_1, and B_2 interpolated (MUTCI) to the bases of the characteristics, as derived below. For one-dimensional ($\partial/\partial x_2 = \partial/\partial x_3 = 0$) incompressible flow ($\nabla \cdot \boldsymbol{v} = 0$), the 2-components of Euler's equation (eq. [2]) and the induction equation (eq. [4]) may be written

$$\frac{\partial v_2}{\partial t} + v_1 \frac{\partial v_2}{\partial x_1} = \frac{B_1}{\rho} \frac{\partial B_2}{\partial x_1} , \tag{40}$$

$$\frac{\partial B_2}{\partial t} + v_1 \frac{\partial B_2}{\partial x_1} = B_1 \frac{\partial v_2}{\partial x_1} . \tag{41}$$

Note that the assumption of incompressibility is justified on the grounds that the compressional terms have already been accounted for in the source step (§ 2.2). Thus, this assumption does *not* restrict this method to compressible flow. Adding and subtracting equations (40) and (41) yield the *characteristic equations*:

$$\frac{D^{\pm}v_2}{Dt} \pm \frac{1}{\sqrt{\rho}} \frac{D^{\pm}B_2}{Dt} = 0 , \tag{42}$$

where

$$\frac{D^{\pm}}{Dt} \equiv \frac{\partial}{\partial t} + (v_1 \mp a_1) \frac{\partial}{\partial x_1} \qquad \text{(Eulerian derivative)} , \tag{43}$$

and where $a_1 \equiv B_1/\rho^{1/2}$. The quantities $c_1^{\pm} = v_1 \mp a_1$ are the *characteristic velocities* along the *characteristic paths* ($C_1^{\pm}$) in incompressible MHD flow. Differencing equations (42) yields

$$v_2^* - v_2^+ + \frac{1}{\sqrt{\rho}} (B_2^* - B_2^+) = 0 , \tag{44}$$

$$v_2^* - v_2^- - \frac{1}{\sqrt{\rho}} (B_2^* - B_2^-) = 0 , \tag{45}$$

where $v_2^{\pm}$ ($B_2^{\pm}$) are MUTCI of v_2 (B_2) to the bases of $C_1^{\pm}$ [i.e., where the characteristics $C_1^{\pm}$ intersect the current (1, 2)-plane (at time step n), as depicted by the (2 + 1)-dimensional spacetime diagram in Fig. 4], upwinded in the characteristic velocities ($c_1^{\pm}$).

Solving equations (44) and (45) for the unknown quantities v_2^* and B_2^* yields

$$v_2^* = \frac{1}{2}\left[v_2^+ + v_2^- + \frac{1}{\sqrt{\rho}} (B_2^+ - B_2^-) \right], \tag{46}$$

$$B_2^* = \tfrac{1}{2}[B_2^+ + B_2^- + \sqrt{\rho}(v_2^+ - v_2^-)] . \tag{47}$$

In order to find the bases of $C_1^{\pm}$, MoC uses 2-point averages to estimate *preliminary* values of the characteristic velocities, $c_1^{\pm}$, namely,

$$c_1^{\pm} = \langle v_1 \rangle_2 \mp \frac{1}{\sqrt{\rho}} \langle B_1 \rangle_2 . \tag{48}$$

An entirely analogous procedure is used to find v_1^* and B_1^* and the four starred values are used to determine ϵ_3 (eq. [39]).

The original design of MoC (SNb) did not perform momentum transport simultaneously with magnetic induction. Nevertheless, the transverse Lorentz acceleration was performed as a part of the overall Eulerian MoC step. With hindsight, this resulted in the asymmetric behavior of forward and backward-moving Alfvén waves computed by MoC in a moving medium seen in the lower panels of Figure 19 in SNb. To correct this problem, the MoC has since been modified so that a separate Lagrangian MoC step is performed to estimate B_1^* and B_2^* to be used exclusively for the transverse Lorentz accelerations (J. Stone 1992, private

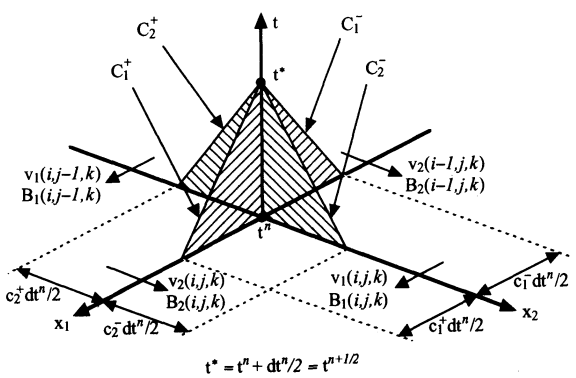

FIG. 4.—A (2 + 1) spacetime diagram showing Lagrangian-like characteristics (i.e., characteristics which straddle the interface) projected back in time from some advanced time t^* to the current time step t^n. In the MoC scheme, values for v_2 and B_2 are interpolated to the bases of the C_1^+ and C_1^- characteristics as determined from *preliminary* estimates (zonal averages) for the characteristic velocities. Similarly, v_1 and B_1 are interpolated to the bases of the C_2^+ and C_2^- characteristics. These interpolated values ($v_2^{\pm}$, $B_2^{\pm}$, $v_1^{\pm}$, and $B_1^{\pm}$) are then used to generate values for v_2^*, B_2^*, v_1^*, and B_1^* (see text). The "starred" values could then be used to generate *secondary* estimates for the characteristic velocities which, in general, are different from the preliminary values. Conversely, the CMoC evaluates the four characteristic velocities implicitly rendering identical preliminary and secondary estimates for the characteristic velocities.

communication). This restores the expected symmetry between forward- and backward-moving Alfvén waves. A Lagrangian MoC step is performed by replacing equation (43) with

$$\frac{D^{\pm}}{Dt} \equiv \frac{\partial}{\partial t} \mp a_1 \frac{\partial}{\partial x_1} \qquad \text{(Lagrangian derivative)} . \tag{49}$$

In this case, the characteristics are determined by the Alfvén speed alone, yielding different MUTCI values for $v_a^{\mp}$ and $B_a^{\pm}$ ($a = 1, 2$) than those used to compute the emf's. Since the MoC step is the most expensive step computationally in the MHD cycle, performing both an Eulerian and a Lagrangian MoC calculation dramatically decreases the efficiency of the algorithm.

The bottom panels of Figure 3 show the one-dimensional Alfvén wave solution as determined by the MoC described above. One can readily see the vast improvement over the original CT scheme as outlined in § 3.1 (Fig. 3, top panels).

An alternative modification to the MoC scheme would be to use v_1^* and v_2^* for both the magnetic induction *and* the momentum transport steps, thereby performing induction and transport simultaneously. In this construct, the transverse Lorentz acceleration step may be and, indeed, must be performed in the Eulerian frame of reference. Thus, the same values for B_1^* and B_2^* must be used for the induction and the Lorentz acceleration steps, obviating the need for separate Lagrangian and Eulerian MoC calculations. This approach is used successfully in the CMoC scheme discussed in § 3.3.

While the MoC works extremely well in one-dimension, it has been observed to exhibit an *explosive* growth of weak magnetic fields in multidimensions. Consider equation (47) and the case where the bases of both characteristics $C_1^{\pm}$ lie on the same side of a zone interface (Fig. 5*a*). In this situation, all terms in B_2^*, including the $v_2^+ - v_2^-$ term, are proportional to the Alfvén speed (much less than the flow velocity by assumption of a weak magnetic field) as desired. Conversely, if $C_1^{\pm}$ straddle the interface (Fig. 5*b*), the $v_2^+ - v_2^-$ term will include the discontinuity (as required by monotonicity) in the piecewise linear interpolation functions representing the internal structures of v_2 within the neighboring zones. Since the discontinuity may be of order v_2, B_2^* may be of order v_2 rather than a_2. Now, in order for $C_1^{\pm}$ to straddle the interface in the first place, $\langle v_1 \rangle_2 < \langle a_1 \rangle_2$, which always has a finite probability of occurring at any given zone interface even for weak magnetic fields, especially across shear layers where neighboring zones are predisposed to having oppositely directed flows. But this need not imply $v_1^* \lesssim B_1^*/\rho^{1/2}$. In fact, v_1^* is not constrained by $\langle v_1 \rangle_2$ (even though they are estimates of the same quantity at the same location on the grid), and v_1^* could still be of order v_1. Thus, in equation (39), the $v_1 B_2$ term in ϵ_3 could be proportional to $v_1 v_2$ rather than $v_1 a_2$, as required if the magnetic field is to remain weak. In a system with an otherwise dynamically insignificant magnetic field, such a spurious ϵ_3 could generate an anomalous and possibly dynamically important magnetic flux loop in a single time step (thus the designation "explosive," see Fig. 6), thereby destroying the integrity of the solution. A practical example of where this problem *dominates* the magnetic field structure is given in § 4.3.

3.3. *The Consistent Method of Characteristics*

The CMoC was designed to cure the explosive "instability" of the MoC. It does so by ensuring v_1^* is of order a_1 if B_2^* is of order v_2 (e.g., because of straddling characteristics). Thus, the *product* $v_1^* B_2^*$ in equation (39) will still be of the order of a flow speed times an Alfvén speed. This is accomplished by determining the characteristic speeds *implicitly* so that the characteristic velocities used to

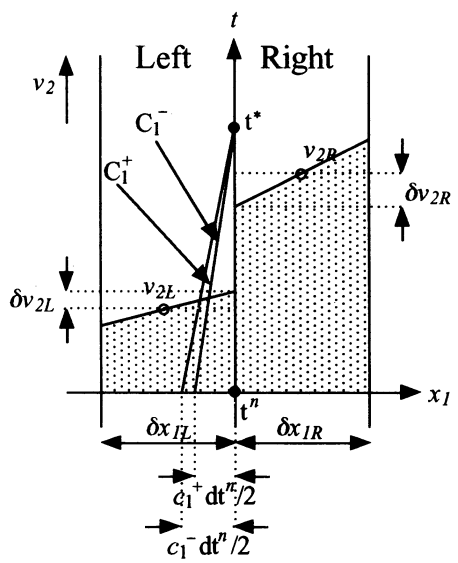

FIG. 5*a*

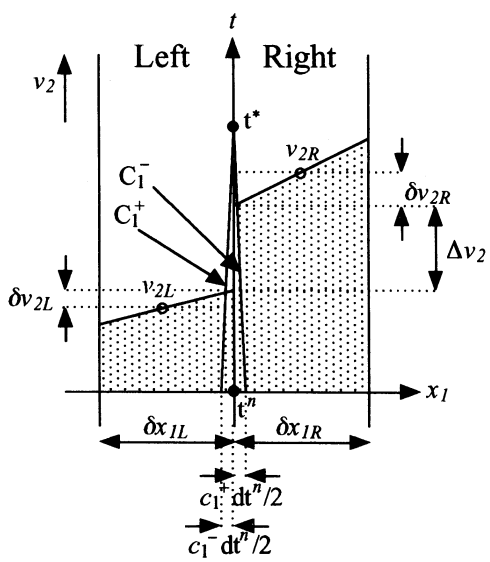

FIG. 5*b*

FIG. 5.—(*a*) Depiction of Eulerian-like characteristics which fall on the same side of the interface. The internal piecewise linear structure for v_2 on either side of the interface are shown as well. In this case, all terms in B_2^* (eq. [47]) are proportional to the Alfvén velocity, including the difference $v_2^+ - v_2^-$ (because the bases of the characteristics are separated by a distance proportional to the Alfvén speed). (*b*) Depiction of Lagrangian-like characteristics which straddle the interface. In this case, the difference $v_2^+ - v_2^-$ contains the term Δv_2 (introduced by monotonicity constraints), which, in general, is proportional to the flow velocity, not the Alfvén velocity. Thus, the estimate for B_2^* will be corrupted for sub-Alfvénic flow.

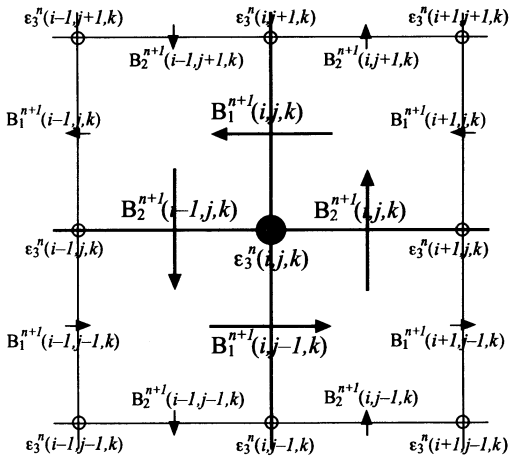

FIG. 6.—An anomalously high ϵ_3 (*large black dot*) will generate an anomalously strong magnetic flux loop encircling the zone edge on which the "bad" *emf* resides. This flux loop, if dynamically important, can spread its effect throughout the grid on dynamical timescales.

determine the locations of the bases of $C_1^{\pm}$ are given by

$$c_a^{\pm} = v_a^* \mp \frac{B_a^*}{\sqrt{\rho}}, \qquad a = 1, 2 \tag{50}$$

rather than by equation (48).

Combining equations (50) with equations (46) and (47), one gets two pairs of coupled algebraic equations:

$$c_1^- = v_1(c_2^+) + B_1(c_2^+)/\sqrt{\rho}\,, \tag{51}$$

$$c_2^+ = v_2(c_1^-) - B_2(c_1^-)/\sqrt{\rho}\,, \tag{52}$$

and

$$c_1^+ = v_1(c_2^-) - B_1(c_2^-)/\sqrt{\rho}\,, \tag{53}$$

$$c_2^- = v_2(c_1^+) + B_2(c_1^+)/\sqrt{\rho}\,, \tag{54}$$

where $v_a^{\pm}$, $B_a^{\pm}$ $(a = 1, 2)$ have been written explicitly as $v_a(c_b^{\pm})$, $B_a(c_b^{\pm})$ $(b = 3 - a)$ to indicate how the interpolations depend upon the characteristic velocities.

Equations (51) and (52) may be solved implicitly for c_1^- and c_2^+ given the interpolation functions $v_1(c_2^+)$, etc. Similarly, equations (53) and (54) may be solved implicitly for c_1^+ and c_2^-. With estimates of the four characteristic velocities, the "starred" values may be determined by inverting equations (50), which are then used to evaluate ϵ_3 (eq. [39]).

To proceed further, one must generate explicit expressions for c_1^- and c_2^+ from equations (51) and (52), and likewise c_1^+ and c_2^- from equations (53) and (54). This task is confounded by the fact that the functional forms of $v_1(c_2^+)$, etc. (interpolation functions [MUTCI] upwinded in the argument) depend upon the signs of c_1^- and c_2^+, which, of course, are not known until equations (51) and (52) are solved! In particular, the van Leer MUTCI scheme (1977) as given by equation (26) but recast with variables and nomenclature used in this subsection is

$$Q_a^{\pm} \equiv Q_a(c_b^{\pm}) = \begin{cases} Q_{a,L} + \delta Q_{a,L}\left(1 - \dfrac{c_b^{\pm}\delta t}{\delta x_{b,L}}\right), & (c_b^{\pm} \geq 0)\,, \\ Q_{a,R} - \delta Q_{a,R}\left(1 + \dfrac{c_b^{\pm}\delta t}{\delta x_{b,R}}\right), & (c_b^{\pm} < 0)\,, \end{cases} \tag{55}$$

where $Q = v$, B and the subscripts L and R designate whether the quantities are from the left or the right of the interface, respectively; $\delta Q_{a,L}$ and $\delta Q_{a,R}$ are the van Leer differences across the left and right zones, respectively (eq. [27]).

Substituting equations (55) in equations (51) and (52) leads to four "candidate" values for each of the characteristics c_1^- and c_2^+, depending upon the signs that c_1^- and c_2^+ end up having. These four candidate values may be written in the compact form

$$c^-_{1,s_1,s_2} = \frac{q^+_{1,s_1} - q^-_{2,s_2}\delta q^+_{1,s_1}}{1 - \delta q^+_{1,s_1}\delta q^-_{2,s_2}}, \tag{56}$$

$$c^+_{2,s_1,s_2} = \frac{q^-_{2,s_2} - q^+_{1,s_1}\delta q^-_{2,s_2}}{1 - \delta q^-_{2,s_2}\delta q^+_{1,s_1}}, \tag{57}$$

where $S_1 = L, R; S_2 = L, R$; and

$$q^{\pm}_{a,S_a} = \bar{v}_{a,S_a} \pm \bar{B}_{a,S_a}/\sqrt{\rho}\,, \tag{58}$$

$$\delta q^{\pm}_{a,S_a} = \phi_{a,S_a} \pm \beta_{a,S_a}/\sqrt{\rho}\,, \tag{59}$$

and

$$\bar{v}_{a,S_a} = v_{a,S_a} + \mathscr{Z}_a \delta v_{a,S_a}\,, \tag{60}$$

$$\bar{B}_{a,S_a} = B_{a,S_a} + \mathscr{Z}_a \delta B_{a,S_a}\,, \tag{61}$$

$$\phi_{a,S_a} = \delta v_{a,S_a}\, \delta t/\delta x_{b,Sa}\,, \tag{62}$$

$$\beta_{a,S_a} = \delta B_{a,S_a}\, \delta t/\delta x_{b,S_a}\,, \tag{63}$$

where $\delta v_{a,S_a}$ and $\delta B_{a,S_a}$ are the van Leer differences in v_a and B_a, respectively, on side $S_a (= L, R)$ (e.g., eq. [27]), and where $a = 1, 2$; $b = 3 - a$; $\mathscr{Z}_a = +1(-1)$ if $S_a = L(R)$.

Equations (56) and (57) generate four possible pairs of values for the characteristic speeds c_1^- and c_2^+, namely,

Case A: $(c^-_{1,L,L}, c^+_{2,L,L})$, Case B: $(c^-_{1,L,R}, c^+_{2,L,R})$,

Case C: $(c^-_{1,R,L}, c^+_{2,R,L})$, Case D: $(c^-_{1,R,R}, c^+_{2,R,R})$.

In order for any of these pairs to be considered further, both speeds in a given pair must be simultaneously upwinded, as defined by equation (55). This constraint may be visualized on a "(c_1^-, c_2^+)-plane" as shown in Figure 7, in which, for illustration purposes, all estimates of the characteristic speeds are positive (i.e., 1-velocities point to the right, 2-velocities point up). Since velocities estimated from the left (right) must be positive (negative) to be upwinded (i.e., pointing to the interface from their offset positions), only quadrant A in Figure 7 contains simultaneously upwinded estimates of (c_1^-, c_2^+). Thus, case A would be selected as the only "upwinded quadrant."

For the most part, one and only one of the four cases A, B, C, and D above will be upwinded. In this event, the job is done, and (c_1^-, c_2^+) is set to $(c^-_{1,S_1,S_2}, c^+_{2,S_1,S_2})$ in the upwinded quadrant. However, in some cases there may be 2, 3, 4, or even no upwinded quadrants. For no upwinded quadrants (c_1^-, c_2^+) is set to (0, 0). For multiple upwinded quadrants, a "zone-of-dependence" average (as illustrated in Fig. 8) is performed on all the upwinded values, with the proviso that quadrants upwinded in only one of the (c_1^-, c_2^+)- and (c_1^+, c_2^-)-planes are severely weighted down relative to quadrants upwinded in both planes. Note that this weighting should not be zero in case there are no common upwinded quadrants in the two planes. Obviously, there is no unique prescription for a zone-of-dependence average, but a form that works well is as follows:

$$c_1^{\mp} = \frac{1}{\mathscr{W}^{\mp}_{1,T}} \sum_{S_1=L,R} \sum_{S_2=L,R} \mathscr{W}^{\mp}_{1,S_1,S_2}\, c^{\mp}_{1,S_1,S_2}\,, \tag{64}$$

$$c_2^{\pm} = \frac{1}{\mathscr{W}^{\pm}_{2,T}} \sum_{S_1=L,R} \sum_{S_2=L,R} \mathscr{W}^{\pm}_{2,S_1,S_2}\, c^{\pm}_{2,S_1,S_2}\,, \tag{65}$$

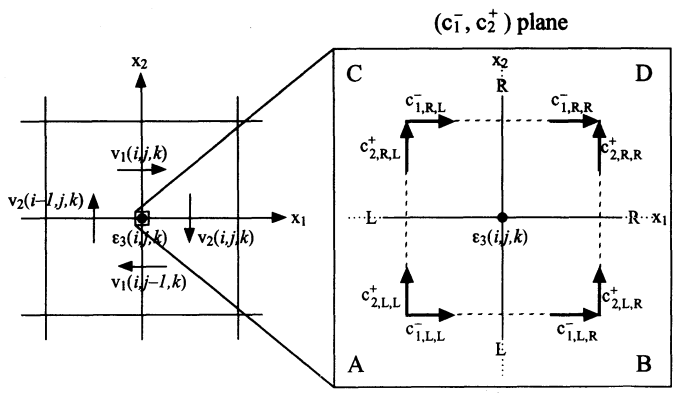

FIG. 7.—An illustration of the concept of "upwinded quadrants." From the text, c_1^- and c_2^+ are coupled, and c_1^+ and c_2^- are coupled. In this diagram, the coupling between c_1^- and c_2^+ is considered, whence the designation "(c_1^-, c_2^+)-plane." On the left is an edge-centered view of four neighboring zones with the nearest velocities labeled. The magnetic fields (the Alfvén velocities) are cospatial with the labeled flow velocities. On the right is a blowup of the immediate vicinity of the zone corner. With respect to the zone corner, interpolations may be performed from either the left (L) or the right (R) in the 1-direction and from the bottom (i.e., left, L) or the top (i.e., right, R) in the 2-direction. This results in four possibilities for the values of c_1^- and c_2^+, labeled according to whether interpolations were performed from the left or right in each of the 1- and 2-directions. Offsetting each possibility from the corner in the diagram is done as a visual aid and is not meant to imply the four possible values are at slightly different locations. "Upwinded quadrants" are readily identified from such a diagram: those quadrants in which the vector tails meet are upwinded; all others are not. Thus, in the diagram as shown, only quadrant A is upwinded.

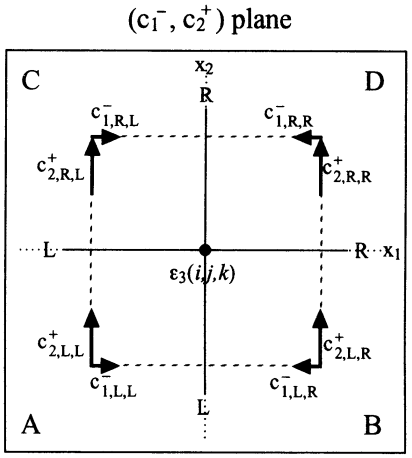

FIG. 8a

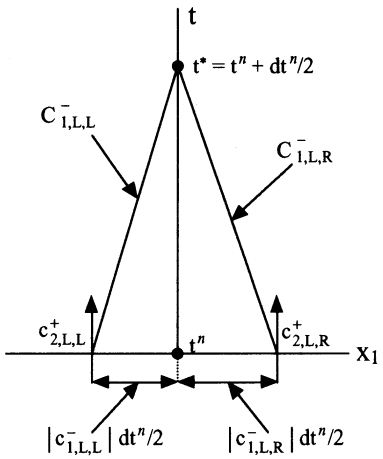

FIG. 8b

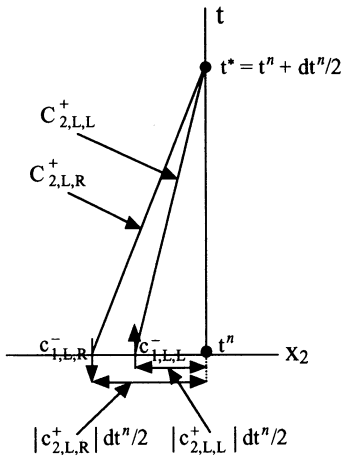

FIG. 8c

FIG. 8.—(*a*) A (c_1^-, c_2^+)-plane with two upwinded quadrants. In this example, the sign of c_1^- depends on whether the interpolation was carried out from the left or the right side of the 1-interface. This has led to two upwinded quadrants, A and B. (*b*) As there are two upwinded quadrants, both have valid "claims" to being the direction from which interpolations should be performed. In a "zone-of-dependence" averaging, the candidate values for c_2^+ (namely, $c^+_{2,L,L}$ and $c^+_{2,L,R}$) are weighted with the baselines of the characteristics to which they are interpolated (thus by $c^-_{1,L,L}$ and $c^-_{1,L,R}$ respectively). (*c*) Candidate values for c_1^- (namely, $c^-_{1,L,L}$ and $c^-_{1,L,R}$) are weighted with the baselines of the characteristics to which they are interpolated (thus by $c^+_{2,L,L}$ and $c^+_{2,L,R}$, respectively).

where the weighting factors are given by

$$\mathcal{W}^{\pm}_{a,S_1,S_2} = \mathcal{W}_{S_1,S_2} |\, c^{\mp}_{b,S_1,S_2} \,|\,, \tag{66}$$

$$\mathcal{W}_{S_1,S_2} = \begin{cases} 0\,, & \text{(quadrant is not upwinded)}\,, \\ 1\,, & \text{(upwinded quadrant in just one plane)}\,, \\ 10^{13}\,, & \text{(upwinded quadrant in both planes)}\,, \end{cases} \tag{67}$$

$$\mathcal{W}^{\pm}_{a,T} = \sum_{S_1=L,R} \sum_{S_2=L,R} \mathcal{W}^{\pm}_{a,S_1,S_2}\,. \tag{68}$$

The choice of 10^{13} assumes 8 byte machine "words" (single precision on Crays, double precision on most other platforms). For 4 byte "words," this factor should be reduced to 10^7.

When only one of the quadrants is upwinded, this scheme always selects the correct quadrant. More important, this scheme maintains smooth, monotonic *emf* profiles even when one or more of the zones along the profile has characteristics straddling the interface and/or multiple upwinded quadrants. This is a critical test of the scheme's generality.

With the characteristic velocities so determined, one solves equation (50) for the starred values. Thus

$$v_a^* = \tfrac{1}{2}(c_a^- + c_a^+)\,, \tag{69}$$

$$B_a^* = \frac{\sqrt{\rho}}{2}(c_a^- - c_a^+)\,, \tag{70}$$

where $a = 1, 2$. Note that for highly super-Alfvénic flow, $c_a^- - c_a^+ \ll c_a^-$. Thus, the quantity B_a^* may be dominated by numerical round-off errors. The simplest way to avoid this circumstance is to avoid setting problems in which

$$\log_{10}(v_{\text{flow}}) - \log_{10}(v_{\text{Alfvén}}) \lesssim \tfrac{1}{2}(\text{number of available significant figures})\,, \tag{71}$$

which, for 8 byte "words," allows for a 10^6-10^7 ratio between the flow velocity and the Alfvén velocity. This should be adequate for most purposes. If higher dynamic ranges cannot be avoided, then instead of constructing "candidate" characteristic speeds (eqs. [56] and [57]), "candidate" values for v^* and B^* are generated directly, and the weighting factors given by equations (66), (67), and (68) are applied to these to determine the final values for the B^*'s and/or v^*'s. This process involves significantly more computations but can accommodate arbitrary ratios between the flow and Alfvén velocities. Further details are omitted in the interest of brevity and can be obtained from the author directly if desired.

The starred values (v_1^*, v_2^*, B_1^*, and B_2^*) are the final estimates of the associated flow variables at the 3-edge and are used to estimate ϵ_3 directly (eq. [39]). Because the starred values are obtained implicitly, the product $v_a^* B_b^*$ is always of the order of a flow velocity times an Alfvén velocity, thus eliminating the explosive instability present in the MoC. Note that v_a^* may be of the order of the Alfvén velocity, and $B_b^*/\rho^{1/2}$ may be of the order of the flow velocity. Such a "virtual exchange of energies" can be tolerated since the CMoC guarantees that the *product* $v_a^* B_b^*$ is properly behaved. In addition, such "virtual exchanges" do not introduce spurious extrema or discontinuities into the *emf* profiles, thus leaving the physical solution unaffected.

In addition to determining ϵ_3, the starred values may be used to determine the transverse Lorentz forces and the transverse momentum fluxes for s_1 and s_2 within the (1, 2)-plane. This is outlined below. Recall that both the MoC and the CMoC are based upon the characteristics of *incompressible* flow. Therefore, the terms governing the propagation of transverse waves (i.e., Alfvén

waves) are performed independently of the compressional terms. Accordingly, compressional momentum transport is performed in a separate transport step (discussed below), while the compressional Lorentz forces are accounted for in the source step (§ 2.2, eq. [16]).

Note that CMoC determines the starred values v_1^*, B_2^*, v_2^*, and B_1^* self-consistently within a plane defined by a constant 3-index (k) *before* ϵ_3 is evaluated and before the transverse Lorentz forces and momentum fluxes acting within the (1, 2)-plane are applied. In this way, CMoC is a "planar-split" scheme, making it fundamentally different from the more traditional "directional-spit" schemes such as the MoC, Godunov-type schemes, and others. Directional-split schemes perform interpolations along a line and thus generate consistent fluxes and emf's in only one dimension at a time. For the most part (and certainly for one-dimensional problems), this is a reasonable approximation to make. However, as shown in § 4, there are situations in multidimensional MHD where this approach leads to disaster. It seems clear that the planar-split nature of the CMoC is central to its ability to treat the curl operator in equation (4) accurately. After all, each component of the curl operates within a *plane* [e.g., $(\nabla \times)_3 = \partial_1 \boldsymbol{i} \times - \partial_2 \boldsymbol{j} \times$] and not along a single *direction*, as do the components of a gradient [e.g., $(\nabla)_3 = \partial_3 \boldsymbol{k}$] or the terms of a divergence [e.g., $(\nabla \cdot)_3 = \partial_3 \boldsymbol{k} \cdot$].

3.3.1. *Applying Transverse Lorentz Forces to s_2 and s_1*

The transverse Lorentz force on s_2 in the 1-direction and on s_1 in the 2-direction are given by (see Fig. 9)

$$s_2^{n,S}(i, j, k) = s_2^{n,S}(i, j, k) + dt^n \frac{[B_1^*(i + 1, j, k) + B_1^*(i, j, k)][B_2^*(i + 1, j, k) - B_2^*(i, j, k)]}{2\, dx_{1a}(i)}, \tag{72}$$

$$s_1^{n,S}(i, j, k) = s_1^{n,S}(i, j, k) + dt^n \frac{[B_2^*(i, j + 1, k) + B_2^*(i, j, k)][B_1^*(i, j + 1, k) - B_1^*(i, j, k)]}{2\, dx_{2a}(j)}. \tag{73}$$

The Lorentz force on s_1 in the 1-direction is compressional and is treated in § 2.2 (eq. [16]).

Ideally, the transverse Lorentz acceleration should be performed simultaneously with the evaluation of the *emf*'s. However, introducing the Lorentz terms implicitly into the scheme outlined above would complicate matters beyond reconciliation. Instead, the Lorentz accelerations are applied to the velocities *as* the *emf*'s are estimated. Thus, immediately after the momenta are updated with the transverse Lorentz forces, the velocities are updated (eq. [19]) and then used to estimate the next *emf* component. In this way, the *emf* estimates are at least partially coupled to the transverse Lorentz acceleration. If all Lorentz accelerations are performed *after* the *emf*'s are computed (as in the original MoC scheme; SNb), *multidimensional* Alfvén wave propagation is unstable (see § 4.2).

3.3.2. *Transverse Transport of s_2 and s_1*

Transport of s_2 in the 1-direction and s_1 in the 2-direction are given by (see Fig. 10)

$$s_2^{n,S,T_1}(i, j, k) = s_2^{n,S}(i, j, k) - \frac{\mathscr{S}_{2,1}(i + 1, j, k) - \mathscr{S}_{2,1}(i, j, k)}{dx_{1a}(i)}, \tag{74}$$

$$s_1^{n,S,T_2}(i, j, k) = s_1^{n,S}(i, j, k) - \frac{\mathscr{S}_{1,2}(i, j + 1, k) - \mathscr{S}_{1,2}(i, j, k)}{dx_{2a}(j)}, \tag{75}$$

where the flux of s_2 in the 1-direction ($\mathscr{S}_{2,1}$) and the flux of s_1 in the 2-direction ($\mathscr{S}_{1,2}$) are given by

$$\mathscr{S}_{2,1}(i, j, k) \equiv \tfrac{1}{2}[\mathscr{M}_1(i, j - 1, k) + \mathscr{M}_1(i, j, k)]v_2^*(i, j, k), \tag{76}$$

$$\mathscr{S}_{1,2}(i, j, k) \equiv \tfrac{1}{2}[\mathscr{M}_2(i - 1, j, k) + \mathscr{M}_2(i, j, k)]v_1^*(i, j, k), \tag{77}$$

and where the linear averages of the mass fluxes (eqs. [24] and [33], used for consistent advection in the scalar transport step in

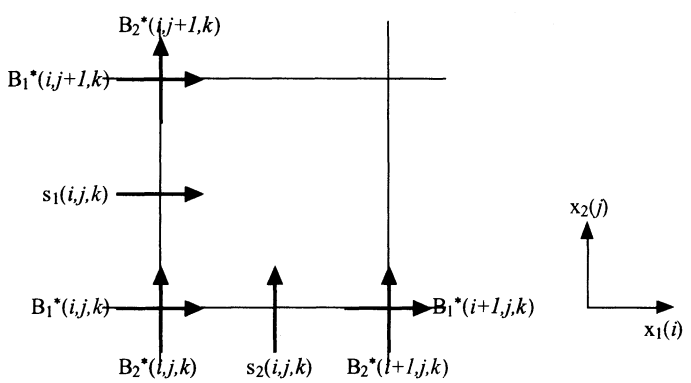

FIG. 9.—Transverse Lorentz forces for s_1 and s_2 are determined from B_1^* and B_2^* (already used to estimate ϵ_3) which are located as shown (eqs [72] and [73])

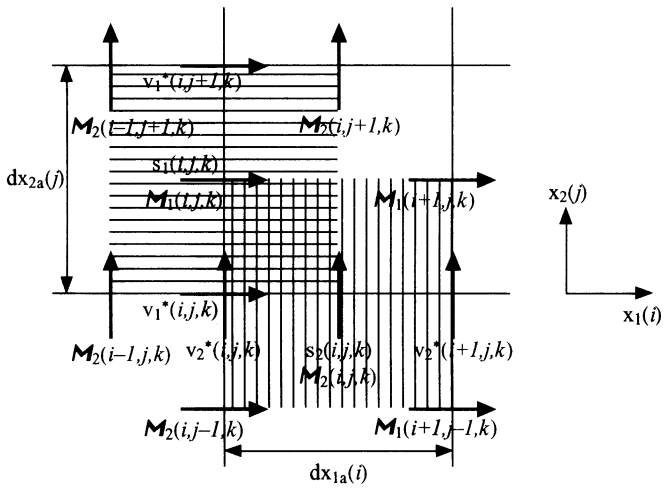

FIG. 10.—In the CMoC scheme, momentum transport is better described as "planar-split" rather than "directional-split." Thus, transport of s_1 in the 2-direction and s_2 in the 1-direction are performed simultaneously as shown. The horizontally hatched area indicates the region into and from which s_1 is transported in the 2-direction. The amount of s_1 transported is determined from v_1^* (already used to estimate ϵ_3) as the interpolation of v_1 at the 2-interface and the 1-average of the mass fluxes $\mathscr{M}_2$ as the agent performing the transport. Similarly, the vertically hatched area indicates the region into and from which s_2 is transported in the 1-direction. The amount of s_2 transported is determined from v_2^* (also used to estimate ϵ_3) as the interpolation of v_2 at the 1-interface and the 2-average of the mass fluxes $\mathscr{M}_1$ as the agent performing the transport.

§ 2.3) ensure proper centering. Therefore, CMoC performs magnetic induction and momentum transport simultaneously, since the starred velocities are also used to construct the momentum fluxes. Unlike the Lorentz acceleration, the velocity should be updated with momentum transport only *after* all the *emf*'s have been evaluated.

3.3.3. *Compressional Transport of* s_1

For convenience, compressional momentum transport (i.e., transporting s_a in the a-direction, $a = 1, 2, 3$) can be performed at the same time as transverse momentum transport, but it is completely independent of the incompressible CMoC process. In fact, compressional momentum transport resembles scalar transport (§ 2.3), except that the momenta are face-centered while the scalar variables are zone-centered.

The transport of s_1 in the 1-direction is given by (see Fig. 11)

$$s_1^{n,S,T_2,T_1}(i,j,k) = s_1^{n,S,T_2}(i,j,k) - \frac{\mathscr{S}_{1,1}(i,j,k) - \mathscr{S}_{1,1}(i-1,j,k)}{dx_{1b}(i)}, \tag{78}$$

where

$$\mathscr{S}_{1,1}(i,j,k) \equiv \frac{1}{2}\left(\mathscr{M}_1(i,j,k) + \mathscr{M}_1(i+1,j,k)\right)\overline{v_1^{n,S}(i,j,k)}^{i}, \tag{79}$$

and where $\overline{v_1^{n,S}(i,j,k)}^{i}$ is the MUTCI of v_1 in the i-direction to the zone centers. Previously, such interpolations have been performed
explicitly (e.g., Norman & Winkler 1986; and SNa), much like MUTCI of the zone-centered scalars to the face-centers (eqs.

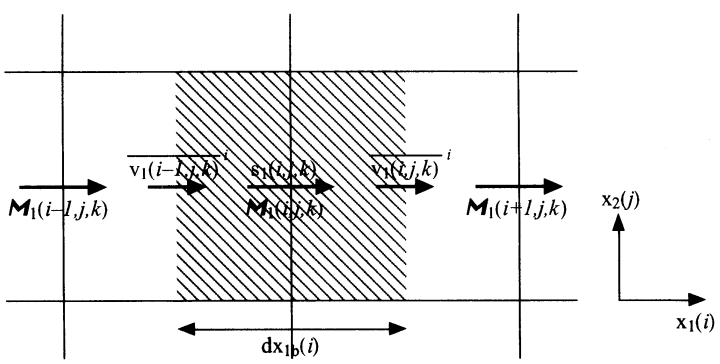

FIG. 11.—Depiction of 1-transport of the 1-momentum. The velocity v_1 is interpolated to the zone centers implicitly independent of the CMoC step (since compressional terms are not involved in the CMoC step). A 1-average of the mass fluxes $\mathscr{M}_1$ is used as the agent performing the transport.

[25]–[28]). Hence, the van Leer second-order explicit MUTCI scheme (1977) for v_1 is given by

$$\overline{v_1^{n,S}(i,j,k)}^{i} = \begin{cases} v_1^{n,S}(i,j,k) + \delta v_1(i,j,k)\left[1 - \dfrac{\xi}{dx_{1b}(i)}\right] & (\xi \geq 0)\,, \\ v_1^{n,S}(i+1,j,k) - \delta v_1(i+1,j,k)\left[1 + \dfrac{\xi}{dx_{1b}(i+1)}\right] & (\xi < 0)\,, \end{cases} \tag{80}$$

where

$$\delta v_1(i,j,k) = \begin{cases} \dfrac{dv_1(i,j,k)dv_1(i-1,j,k)}{dv_1(i,j,k) + dv_1(i-1,j,k)} & [dv_1(i,j,k)\,dv_1(i-1,j,k) > 0]\,, \\ 0 & (\text{otherwise})\,, \end{cases} \tag{81}$$

$$dv_1(i,j,k) \equiv v_1^{n,S}(i+1,j,k) - v_1^{n,S}(i,j,k)\,, \tag{82}$$

and where $\xi \equiv \langle v_1^{n,S}(i,j,k)\rangle_1\, dt^n$, with $\langle v_1^{n,S}(i,j,k)\rangle_1$ being an estimate of v_1 at the zone center for determining upwindedness and time-centering. In an explicit interpolation scheme, $\langle v_1^{n,S}(i,j,k)\rangle_1$ is simply set to a two-point spatial average. Note, however, that $\overline{v_1^{n,S}(i,j,k)}^{i}$ is also an estimate of v_1 at the zone center. Thus, in the spirit of the CMoC, one might set $\langle v_1^{n,S}(i,j,k)\rangle_1 = \overline{v_1^{n,S}(i,j,k)}^{i}$ in equation (80) and solve for $\overline{v_1^{n,S}(i,j,k)}^{i}$. This generates a van Leer second-order *implicit* MUTCI scheme for v_1, namely,

$$\overline{v_1^{n,S}(i,j,k)}^{i} = \begin{cases} v_{1L} & (v_{1L} > 0 \quad \text{and} \quad v_{1R} > 0)\,, \\ v_{1R} & (v_{1L} < 0 \quad \text{and} \quad v_{1R} < 0)\,, \\ 0 & (\text{otherwise})\,, \end{cases} \tag{83}$$

where

$$v_{1L} = \frac{v_1^{n,S}(i,j,k) + \delta v_1(i,j,k)}{1 + \delta v_1(i,j,k)\, dt^n/dx_{1b}(i)}\,, \tag{84}$$

$$v_{1R} = \frac{v_1^{n,S}(i+1,j,k) - \delta v_1(i+1,j,k)}{1 + \delta v_1(i+1,j,k)\, dt^n/dx_{1b}(i+1)}\,, \tag{85}$$

and where $\delta v_1(i,j,k)$ is given by equation (81).

While the implicit MUTCI scheme is perhaps more aesthetically satisfying, the author has found no evidence to suggest that it improves or degrades the accuracy or stability of the compressional transport of momenta. It is presented here as an option only because it follows the spirit of CMoC in which the implicit nature of the interpolation was critical to the solution of the explosive instability in the MoC for the limit of weak magnetic fields.

3.3.4. *Planar-Split on the 3-1 Plane* (ϵ_2)

Completely analogous procedures are followed to obtain v_3^*, B_1^*, v_1^*, and B_3^* at the 2-edge, and thus ϵ_2 may be estimated by equation (39) with an appropriate permutation of the indices and labels. B_3^* and B_1^* at the 2-edge are then used to estimate the transverse Lorentz forces on s_1 in the 3-direction and on s_3 in the 1-direction (eqs. [72] and [73] with indices and labels permuted).

v_3^* and v_1^* at the 2-edge are used to transport s_1 in the 3-direction and s_3 in the 1-direction thus:

$$s_1^{n+1}(i,j,k) = s_1^{n,S,T_2,T_1}(i,j,k) - \frac{\mathscr{S}_{1,3}(i,j,k+1) - \mathscr{S}_{1,3}(i,j,k)}{dx_{3a}(k)}\,, \tag{86}$$

$$s_3^{n,S,T_1}(i,j,k) = s_3^{n,S}(i,j,k) - \frac{\mathscr{S}_{3,1}(i+1,j,k) - \mathscr{S}_{3,1}(i,j,k)}{dx_{1a}(i)}\,. \tag{87}$$

Where, with the appropriate permutation of the indices and labels, $\mathscr{S}_{1,3}(i,j,k)$ and $\mathscr{S}_{3,1}(i,j,k)$ are given by equations (76) and (77), respectively.

Compressional transport of s_3 in the 3-direction is given by

$$s_3^{n,S,T_1,T_3}(i,j,k) = s_3^{n,S,T_1}(i,j,k) - \frac{\mathscr{S}_{3,3}(i,j,k) - \mathscr{S}_{3,3}(i,j,k-1)}{dx_{3b}(k)}\,, \tag{88}$$

where $\mathscr{S}_{3,3}(i,j,k)$ is given by equation (79), again with the appropriate permutation of the indices and labels.

3.3.5. *Planar-Split on the 2-3 Plane* (ϵ_1)

Completely analogous procedures are followed to obtain v_2^*, B_3^*, v_3^*, and B_2^* at the 1-edge, and, thus, ϵ_1 may be estimated by equation (39) with an appropriate permutation of the indices and labels. B_2^* and B_3^* at the 1-edge are then used to estimate the transverse Lorentz forces on s_3 in the 2-direction and on s_2 in the 3-direction (eqs. [72] and [73] with indices and labels permuted).

The starred velocities v_2^* and v_3^* at the 1-edge are used to transport s_3 in the 2-direction and s_2 in the 3-direction thus:

$$s_3{}^{n+1}(i, j, k) = s_3{}^{n,S,T_1,T_3}(i, j, k) - \frac{\mathcal{S}_{3,2}(i, j+1, k) - \mathcal{S}_{3,2}(i, j, k)}{dx_{2a}(j)}, \tag{89}$$

$$s_2{}^{n,S,T_1,T_3}(i, j, k) = s_2{}^{n,S,T_1}(i, j, k) - \frac{\mathcal{S}_{2,3}(i, j, k+1) - \mathcal{S}_{2,3}(i, j, k)}{dx_{3a}(k)}, \tag{90}$$

where, with the appropriate permutation of the indices and labels, $\mathcal{S}_{3,2}(i, j, k)$ and $\mathcal{S}_{2,3}(i, j, k)$ are given by equations (76) and (77), respectively.

Compressional transport of s_2 in the 2-direction is given by

$$s_2{}^{n+1}(i, j, k) = s_2{}^{n,S,T_1,T_3}(i, j, k) - \frac{\mathcal{S}_{2,2}(i, j, k) - \mathcal{S}_{2,2}(i, j-1, k)}{dx_{2b}(j)}, \tag{91}$$

where $\mathcal{S}_{2,2}(i, j, k)$ is given by equation (79), again with the appropriate permutation of the indices and labels.

Note that the CMoC outlined in this subsection is not symmetric under a permutation of the order in which the scheme is planar-split. That is to say, in a nonsymmetric system, computing the *emf*'s in the order ϵ_1–ϵ_2–ϵ_3 will yield slightly different results than if the *emf*'s were computed in the order ϵ_2–ϵ_3–ϵ_1 say. In part, this is because the velocities are Lorentz accelerated *while* the *emf*'s are being estimated, which introduces planar asymmetries in both the *emf*'s and the momentum fluxes. In addition, the momentum fluxes are determined from partially updated mass fluxes. As with transport of scalar quantities (§ 2.3), the author has found no evidence to suggest such asymmetries are at all consequential in a general application. However, in test problems in which symmetry is being tested, cyclically permuting the order in which the *emf*'s are computed (and thus the order in which momenta transport are performed) will improve the apparent symmetry of the numerical solution.

The final step is to use the *emf*'s to update the 1-component of the magnetic field using equation (36), and similar equations (with indices and labels permuted) for the 2- and 3-components of the magnetic field.

The flowchart in Figure 12 illustrates how the author has implemented all the ideas in this paper into a working MHD code (ZEUS-3D), while Figure 13 is a detailed flowchart illustrating the CMoC step discussed specifically in this subsection.

4. NUMERICAL EXAMPLES

The explosive growth of weak magnetic fields in the MoC is multidimensional in nature and thus not illustrated by any of the usual one-dimensional MHD test problems (e.g., Stone et al. 1992; RJ). In fact, the CMoC and the MoC reduce to virtually the same algorithm in one dimension. Nevertheless, it serves as a good introduction to this section to present the CMoC solution of a few one-dimensional test problems. The CMoC has been tested with virtually all the test problems discussed in Stone et al. (1992) and many of those in RJ, all with favorable results.

4.1. *One-dimensional Shock-Tube Tests*

The one-dimensional MHD shock-tube problem of Brio & Wu (1988) has received considerable attention as a standard test for MHD algorithms. Thus, the CMoC calculation of the "Brio & Wu problem" is presented here to "calibrate" the CMoC against other MHD schemes.

The Brio & Wu shock tube is initialized with two distinct left- and right-hand states. A one-dimensional computational grid of 550 uniform Cartesian zones is constructed along the 1-direction with a left-hand state ($\rho = 1$, $p = 1$, $B_1 = \frac{3}{4}$, and $B_2 = 1$)[2] initialized along the first 200 zones, and a right-hand state ($\rho = \frac{4}{5}$, $p = \frac{1}{8}$, $B_1 = \frac{3}{4}$, and $B_2 = -1$) initialized along the remaining 350 zones. The initial values of all remaining flow variables are zero. The adiabatic index is set to 2 (for consistency with Brio & Wu), and the viscous parameters Q_1 and Q_2 (Appendix A) are set to 0.2 and 2.0, respectively. The two states are allowed to interact for a time $t = 80$ in units where the grid domain is $0 < x_1 < 550$. The resulting CMoC solution is shown in Figure 14. The solution is characterized by two fast rarefaction waves, a slow shock, a contact discontinuity, and a "compound wave," all labeled in Figure 14. The compound wave appearing in this solution has been somewhat controversial, although the consensus seems to be that this feature is real. Nevertheless, even the best of the analytic MHD Riemann solvers (RJ) does not include the compound wave as part of the solution to the Brio & Wu problem.

The MHD algorithm of Brio & Wu (1988) is upwinded in all MHD characteristics, including compressional waves. By compression, the characteristics used by CMoC are incompressible, with the compressional terms handled in distinct operator-split steps. Still, there is good agreement between the Brio & Wu solution (Fig. 2 in Brio & Wu 1988) and the CMoC solution (Fig. 14). The most noticeable defects in the CMoC solution are the slight undershoot in the density and pressure at the base of the rarefaction wave in the left-hand state, and the ringing in the velocity and magnetic field in the region between the slow shock and the fast rarefaction in the right-hand state. The former is caused almost entirely by the lack of strict energy conservation, an unfortunate side effect of solving for the internal energy (eq. [3]) rather than the total energy. If, instead, one solves the total energy equation (eq. [115], Appendix B), the undershoot virtually disappears (not shown). The ringing is likely a consequence of upwinding in the incompressible MHD characteristics only and can be suppressed effectively with an appropriate amount of artificial viscosity.

The second one-dimensional shock-tube test problem presented in this section corresponds to Figure 1*a* in RJ.[3] In this problem, a one-dimensional grid of 512 uniform Cartesian zones is constructed along the 1-direction with a left-hand state ($\rho = 1$, $p = 20$,

[2] Magnetic field in units defined by eqs. (7) and (8).

[3] Note that there is a typo in the captions of Figs. 1–5 in RJ. The final variable characterizing the two states is gas pressure (p_g), not total energy (E).

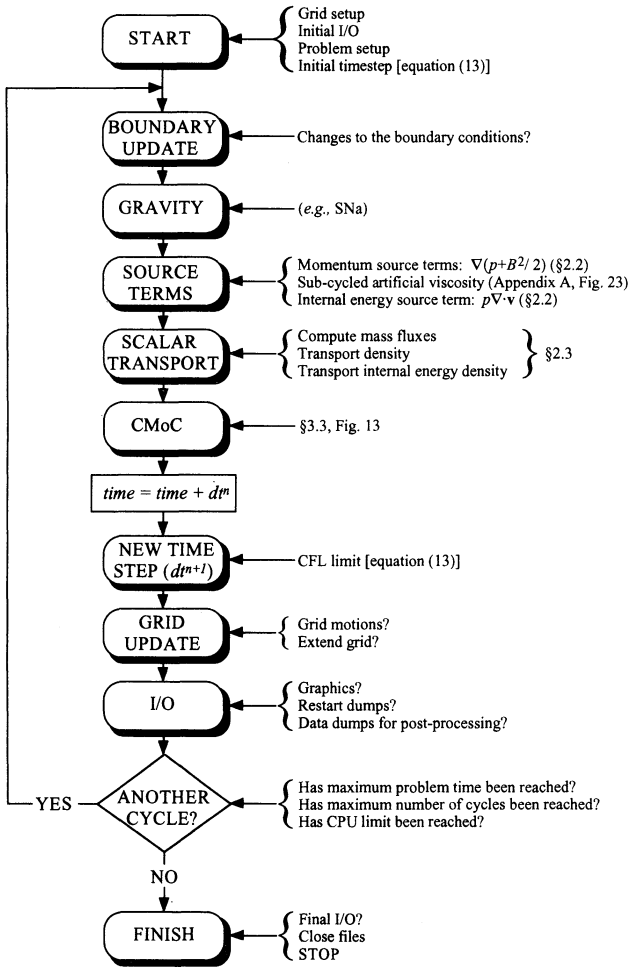

FIG. 12

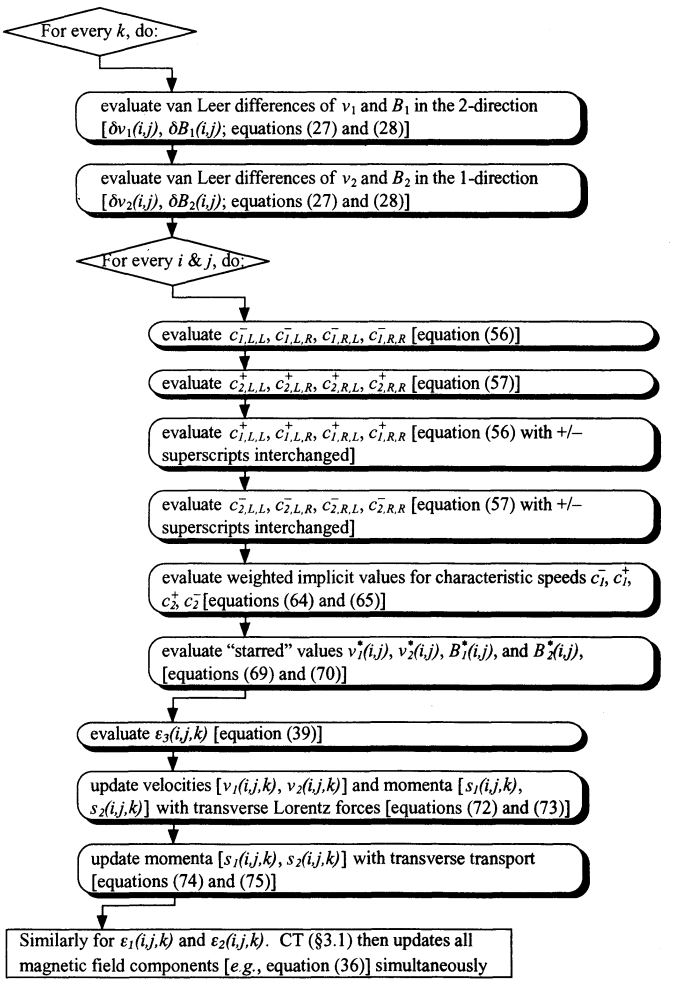

FIG. 13

FIG. 12.—Flowchart of the main loop of the ZEUS-3D code which incorporates the CMoC algorithm into a working multidimensional MHD computer program.

FIG. 13.—Detailed flowchart of the CMoC algorithm to evaluate ϵ_3 (3-component of $\boldsymbol{v} \times \boldsymbol{B}$) as implemented in the ZEUS-3D computer program (§ 3.3). The indices i, j, and k in the diamonds are the coordinates of the three-dimensional arrays. The variables evaluated in the inner loop bubbles can all be represented by scalars, while the variables evaluated in the outer loop bubbles are two- or three-dimensional arrays as indicated by the number of associated indices. Note that similar flowcharts may be constructed for ϵ_1 and ϵ_2, and the order in which these three flowcharts are executed may be permuted from time step to time step to improve numerical symmetry among the three directions.

$v_1 = 10$, and $B_1 = B_2 = 1.41047$) initialized along the first 256 zones, and a right-hand state ($\rho = 1$, $p = 10$, $v_1 = -10$, and $B_1 = B_2 = 1.41047$) initialized along the remaining 256 zones. The adiabatic index is set to 5/3, and the viscous parameters Q_1 and Q_2 (Appendix A) are set to 0.2 and 2.0, respectively. The total energy equation (Appendix B) is used instead of the internal energy equation to improve the accuracy of the solution. The two states are allowed to interact for a time $t = 0.08$ in units where the grid domain is $0 < x_1 < 1$. The resulting CMoC solution shown in Figure 15 is characterized by two fast shocks, a slow rarefaction, a contact discontinuity, and a slow shock. Some differences between the CMoC and RJ solutions exist. The CMoC requires more zones to track the fast shocks, but fewer zones to track the contact discontinuity than RJ's total variation diminishing (TVD) algorithm. As a consequence of the latter, the CMoC produces a spurious undershoot before the contact discontinuity in the transverse velocity and magnetic field. Otherwise the levels produced by the two schemes are virtually identical.

For the third problem, the same grid, adiabatic index, and viscous parameters are used as for the previous problem. The left-hand state ($\rho = 1.08$, $p = 0.95$, $v_1 = 1.2$, $v_2 = 0.01$, $v_3 = 0.5$, $B_1 = B_3 = 0.56419$, and $B_2 = 1.01554$) is initialized along the first 256 zones, and the right-hand state ($\rho = 1$, $p = 1$, $B_1 = B_3 = 0.56419$, and $B_2 = 1.12838$) is initialized along the remaining 256 zones. The internal energy equation is used, since it is adequate for this problem. The two states are allowed to interact for a time $t = 0.2$ in units where the grid domain is $0 < x_1 < 1$. The resulting CMoC solution shown in Figure 16 is characterized by two fast shocks, two rotational discontinuities, two slow shocks, and a contact discontinuity. The differences between the CMoC and RJ solutions are largely cosmetic. The CMoC requires more zones to track the fast shocks and rotational discontinuities (CMoC possesses no contact steepener), but fewer zones to track the slow shocks and the contact discontinuity than RJ's TVD algorithm. Both schemes

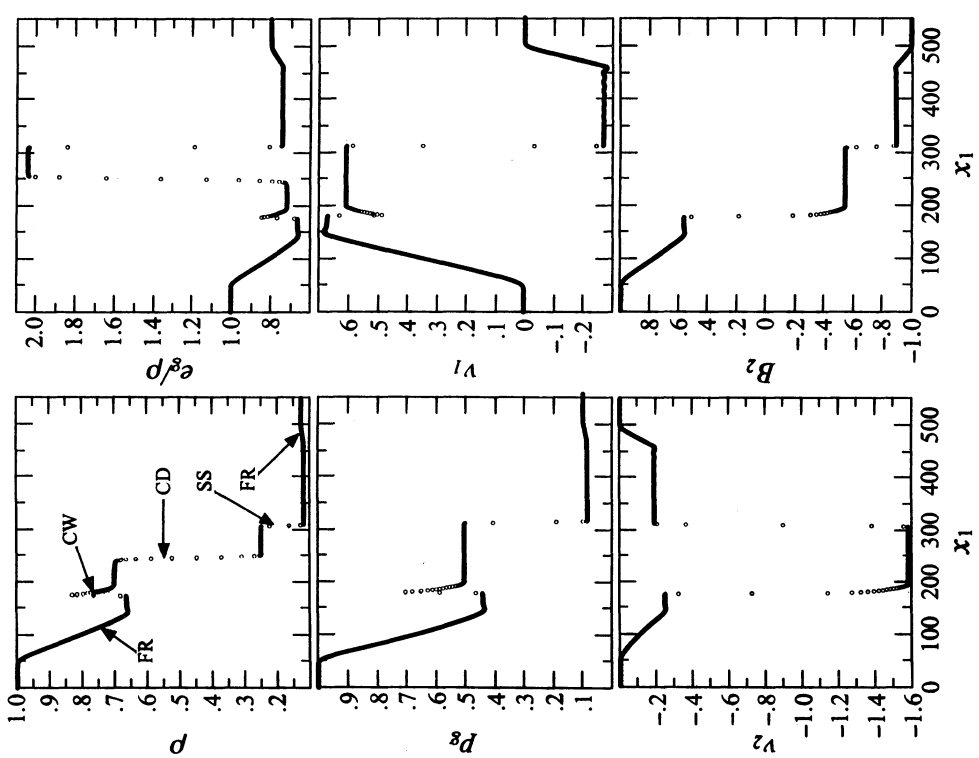

FIG. 14

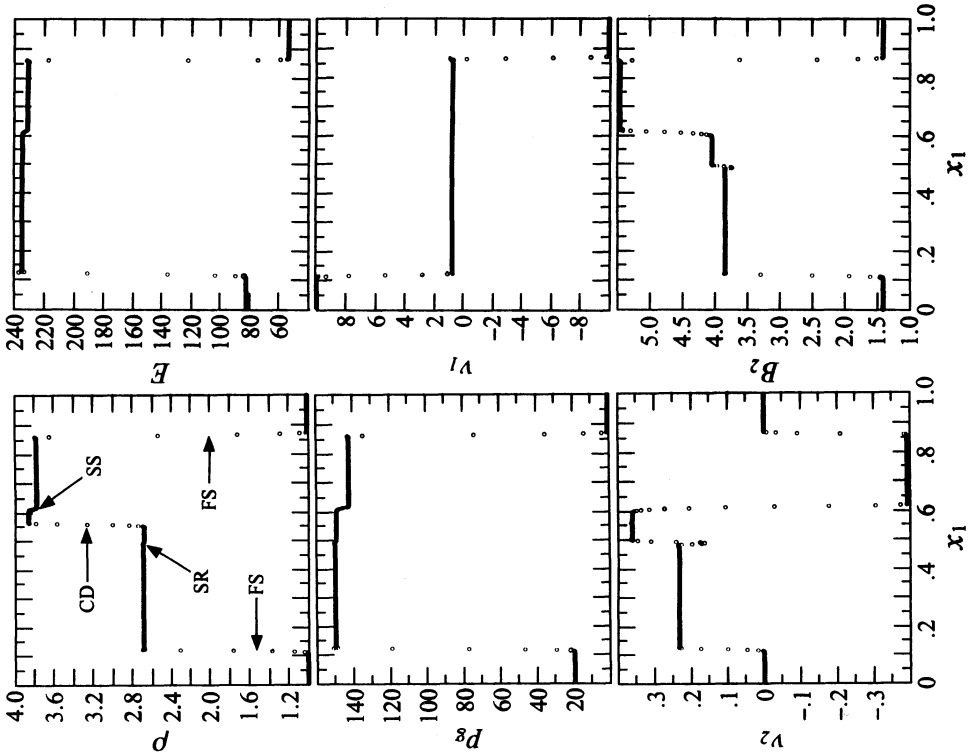

FIG. 15

FIG. 14.—CMoC solution of the "Brio & Wu" problem (Brio & Wu 1988) computed on a one-dimensional grid with 550 zones. Variables clockwise from top right are specific thermal energy (e_g/ρ), 1-velocity (v_1), 2–magnetic field (B_2), 2-velocity (v_2), thermal pressure (p_g), and density (ρ). Features labeled on the density plot include two fast rarefaction waves (FR), a compound wave (CW: slow shock plus a slow rarefaction wave), a contact discontinuity (CD), and a slow shock (SS).

FIG. 15.—CMoC solution of an MHD shock-tube problem described in Dai & Woodward (1994, their Fig. 8) and RJ (their Fig. 1*a*) computed on a one-dimensional grid with 512 zones. Variables clockwise from top right are total energy density (E), 1-velocity (v_1), 2–magnetic field (B_2), 2-velocity (v_2), thermal pressure (p_g), and density (ρ). Features labeled on the density plot include two fast shocks (FS), a slow rarefaction wave (SR), a contact discontinuity (CD), and a slow shock (SS).

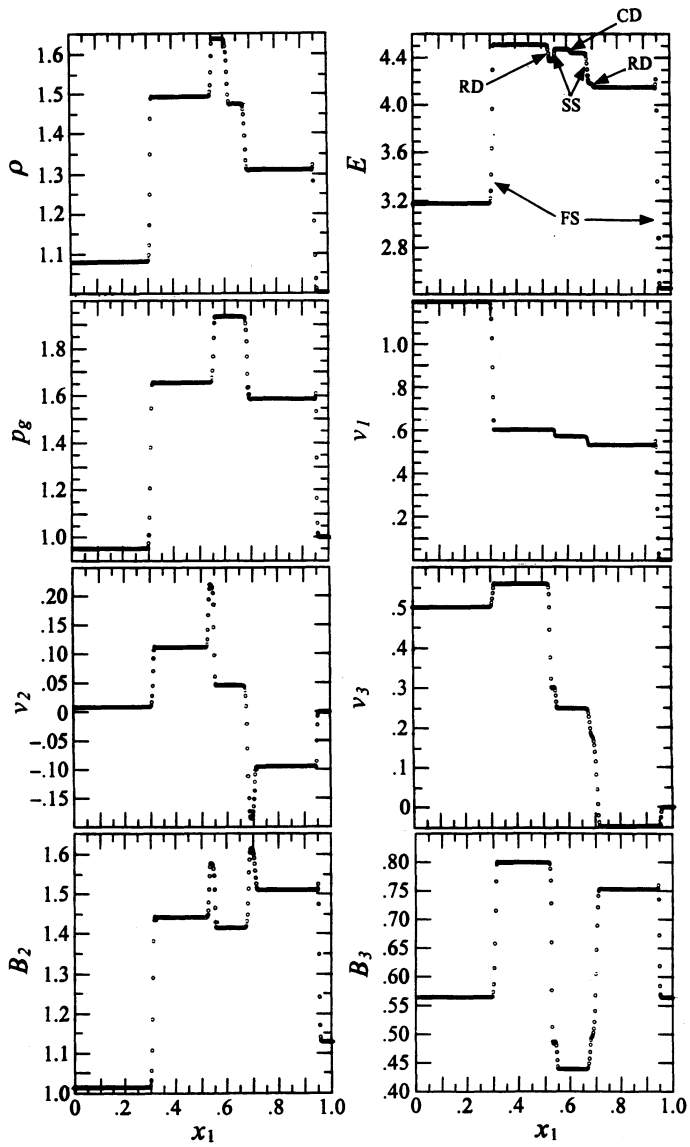

FIG. 16.—CMoC solution of an MHD shock-tube problem described in RJ (their Fig. 2*a*) computed on a one-dimensional grid with 512 zones. Variables clockwise from top right are total energy density (E), 1-velocity (v_1), 3-velocity (v_3), 3–magnetic field (B_3), 2–magnetic field (B_2), 2-velocity (v_2), thermal pressure (p_g), and density (ρ). Features labeled on the total energy plot include two fast shocks (FS), two rotational discontinuities (RD), two slow shocks (SS), and a contact discontinuity (CD).

show small "glitches" in the density and thermal pressure at the location of the rotational discontinuities, and the CMoC exhibits a small overshoot upstream of the fast shock in the right-hand state. Otherwise, the levels produced by the two schemes are virtually identical.

4.2. *Two-dimensional Propagation of Alfvén Wave*

The two-dimensional analog to the one-dimensional Alfvén wave test (Fig. 3) provides a discriminating multidimensional test for CMoC. A circular pulse of velocity perpendicular to the plane of computation is initialized at the center of a 200 × 200 zone grid which contains a uniform magnetic field. Specifically, thoughout the (1, 2)-plane, the density, pressure, and adiabatic index are set to 1, 3/5, and 5/3, respectively. The velocity field is set to zero everywhere, except for a circular region in the center of the grid with a radius of 10 zones in which v_3 (velocity perpendicular to the computational plane) is set to 10^{-3}. As with the one-dimensional solution, the circular pulse in v_3 should be carried along the magnetic field lines at the Alfvén speed intact and undistorted.

Figures 17 and 18 (showing contours of v_3) compare the transport of two-dimensional Alfvén waves by three characteristic-based MHD algorithms, namely, the original MoC (SNb), a modified MoC suggested by J. Hawley (1992, private communication), and the CMoC. The differences among the panels in Figures 17 and 18 are unrelated to the explosive "instability" of the MoC discussed previously. Instead they result from the details of how the transverse Lorentz forces are applied. In the original MoC scheme, transverse Lorentz accelerations (e.g., §§ 3.3.1) are applied to the velocities entirely *after* the *emf*'s have been evaluated. Thus, the velocities used to compute the *emf*'s have no "knowledge" of the transverse Lorentz forces during the current time step. Hawley's

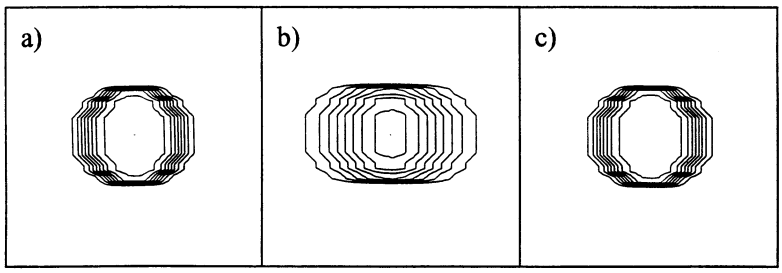

FIG. 17.—Contours of velocity perpendicular to the grid (v_3) of an initially circular Alfvén wave after having traveled approximately 4 pulse diameters along the 1-axis using (*a*) the original MoC (SNb), (*b*) Hawley's modified MoC, and (*c*) the CMoC. Note that the angularity of the contour lines in places is a consequence of trying to resolve a circular pulse on a limited number of Cartesian zones.

modification to the MoC scheme includes applying the transverse Lorentz accelerations to the velocities *before* the *emf*'s are computed. In this case, no "time-centering" of the transverse Lorentz accelerations relative to the determination of the *emf*'s is performed. In the CMoC, the transverse Lorentz accelerations are interleaved with the *emf* evaluations, and the order in which the *emf*'s are estimated is permuted at every time step. This may be regarded as an attempt to "time-center" the transverse Lorentz accelerations and compensate partially for the fact that the Lorentz forces are not applied implicitly with the *emf*'s and momenta transport.

Figure 17 depicts the two-dimensional Alfvén pulse after it has been transported 75 zones along the 1-direction ($\boldsymbol{B} = \boldsymbol{i}$, $v_{\rm Alfven} = 1$) using the three methods discussed above. Note that the diffusion of the pulse is strictly confined to the direction of propagation and is exactly the diffusion seen in Figure 3 (*bottom panels*) when the MoC or the CMoC is used (Figs. 17*a* and 17*c*). Using Hawley's modified MoC (Fig. 17*b*), the diffusion is much greater. In all cases, the pulse is transported stably.

Figure 18 depicts the two-dimensional Alfvén pulse after it has been transported the same distance as Figure 17 but at an angle of 45° with respect to the computational grid ($\boldsymbol{B} = \boldsymbol{i} + \boldsymbol{j}$, $v_{\rm Alfven} = 2^{1/2}$). The circular pulse breaks up into linear striations using the original MoC (Fig. 18*a*) but maintains its circular shape using Hawley's modified MoC (Fig. 18*b*). This gain in stability has come at a great cost in diffusion of the pulse. Using the CMoC, the circular pulse remains stable and is elongated *perpendicular* to the direction of propagation (Fig. 18*c*).

4.3. *Three-dimensional Supersonic Jet*

To date, the author knows of no analytically soluble problem to demonstrate the explosive "instability" of the MoC. The discovery of a canonical test problem for this effect would help enormously in calibrating and comparing this and future MHD algorithms. In fact, the explosive "instability" was uncovered during the execution of three-dimensional computations of astrophysical jets transporting weak magnetic fields, and these are presented here as the definitive discriminant between the MoC and CMoC algorithms.

Because the explosive "instability" is goaded by strong shear layers, the surface of a supersonic jet provides an ideal environment in which to observe magnetic field "explosions" of the MoC type. Figure 19 is a cartoon of a jet computation depicting the anatomy of the jet once it has had time to evolve and affect its environment. This is discussed further in the next section. The jet is light (jet density is 2% of the quiescent ambient) and supersonic (Mach 6). It is initially in pressure balance with a uniform atmosphere and transports an arbitrarily weak magnetic field (originally included to generate synchrotron emissivities and not to affect the dynamics). The jet is computed on a 125 × 80 × 80 Cartesian grid with 10 zones across the jet diameter and is perturbed at the orifice with a 2% helical perturbation to break the azimuthal symmetry. As the jet advances across the grid, it excites a series of shocks both in the ambient medium and within the jet itself. Only the jet material is magnetized.

By tracking (with high temporal resolution) the extrema of all three magnetic field components in the entire grid and the total magnetic energy density integrated over the entire volume, one can observe the MoC explosive instability directly. Figure 20 shows the magnetic field extrema for the first 25% of the simulation as computed with the MoC (Fig. 20*a*) and the CMoC (Fig. 20*b*). The explosive events are unmistakable in Figure 20*a*, with sudden jumps of magnetic field extrema occurring in symmetric pairs (i.e., the

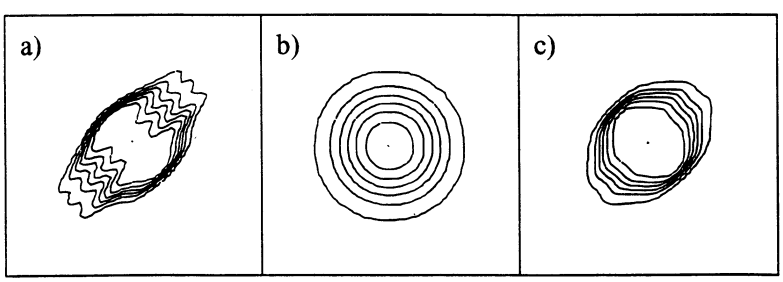

FIG. 18.—Same as Fig. 17, except the circular Alfvén wave propagates at 45° relative to the two-dimensional grid. As discussed in the text, the original MoC destroys the pulse (*a*), Hawley's modified MoC maintains stability but strongly diffuses the pulse (*b*), and the CMoC maintains stability while elongating the pulse primarily in a direction *perpendicular* to the propagation (*c*).

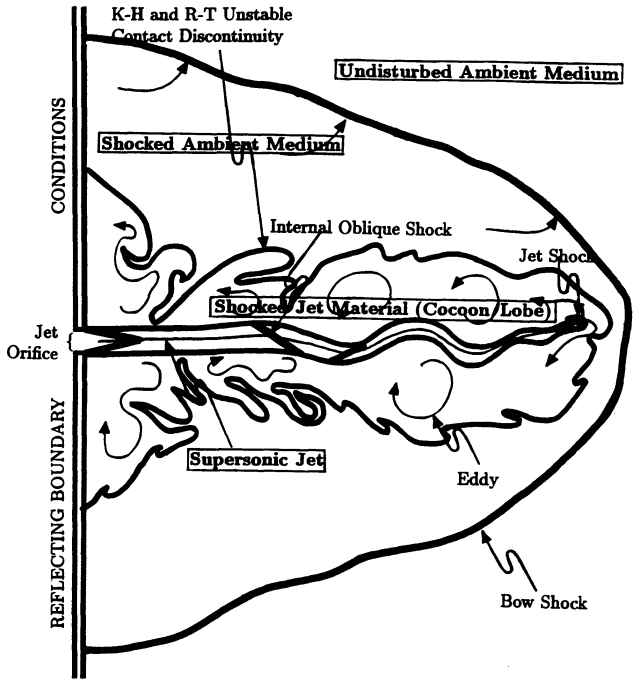

FIG. 19.—Anatomy of the advancing jet in the simulation described in the text. The jet enters from an orifice on the left-hand boundary of the grid. Flow-in boundary conditions are maintained in a circular region on the boundary which forces a supersonic (Mach 6), light ($\rho_{jet}/\rho_{ambient} = 0.02$) jet to propagate into the otherwise quiescent and homogeneous ambient medium. Major features are labeled in the figure.

most positive value and the most negative value simultaneously jumping to comparable absolute values). While not apparent from Figure 20*a*, explosive extrema are always located in neighboring zones and form part of an anomalous flux loop surrounding a spurious *emf*, as discussed in § 2.2 (see Fig. 6). Note, however, that the magnetic field extrema behave much more continuously when computed with the CMoC (Fig. 20*b*), which shows no sign whatsoever of the explosive behavior of the MoC.

The toll exacted from the integrity of the MoC calculation by unchecked and numerous explosive events is readily seen in the total magnetic energy. Figure 21*a* shows the evolution of the total magnetic field energy in the computational domain of the MoC

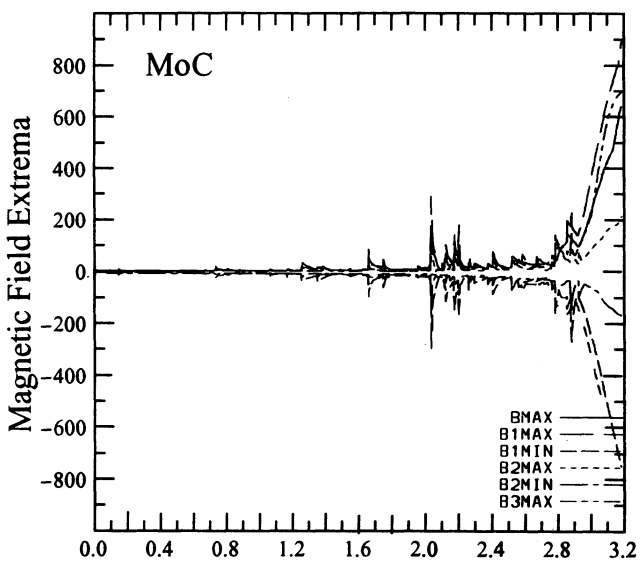

FIG. 20*a*

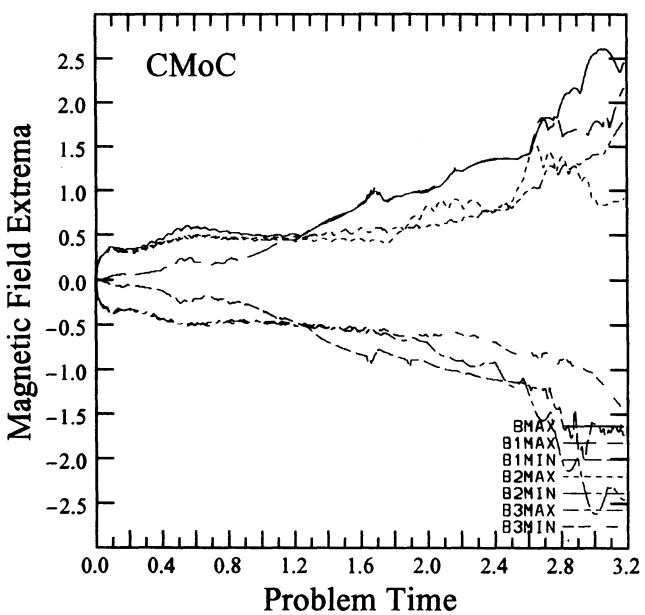

FIG. 20*b*

FIG. 20.—Extrema for the magnetic field components as a function of problem time for the supersonic jet problem described in the text as computed by (*a*) the MoC and (*b*) the CMoC. The same arbitrary units are used on the axes for both panels. The "explosions" are clearly visible in the MoC solution (*opposing spikes*) but are entirely absent in the CMoC solution.

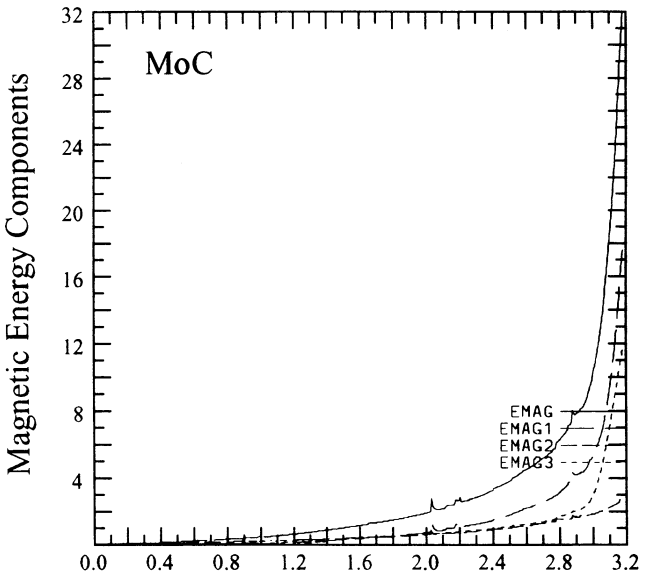

FIG. 21*a*

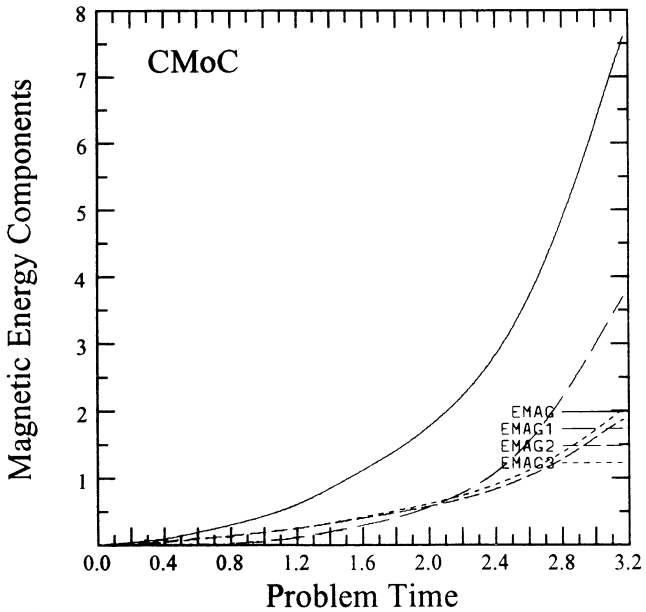

FIG. 21*b*

FIG. 21.—Magnetic field energy density integrated over the entire computational domain for the supersonic jet problem described in the text as computed by (*a*) the MoC and (*b*) the CMoC. The same arbitrary units are used on the axes for both panels. The explosion at $t = 2.05$ in Fig. 20*a* was sufficiently large that the magnetic field energy density in this single zone was comparable to the magnetic energy density integrated over the rest of the grid. Note that by $t = 3.2$ the MoC has generated more than 4 times as much magnetic energy as has the CMoC.

calculation as a function of time. Despite the fact that this is the total magnetic energy integrated over the entire volume, one can still pick out individual explosive events which generate magnetic energy within a pair of zones comparable to that contained by the rest of the grid! Taking the CMoC evolution (Fig. 21*b*) as more realistic, the MoC calculation has apparently exaggerated the total magnetic energy density in the computational volume by several times after only 25% of the simulation was performed. This additional magnetic energy has come at the expense of the kinetic energy in the system. In fact, when the MoC simulation was $\sim 30\%$ complete, an explosive event occurred in which the weak magnetic field (originally, $\beta \equiv 2p/B^2 \sim 10^{10}$) was promoted to $\beta \gtrsim 1$ within a single time step, and the subsequent evolution of this dynamically important "seed" of magnetic field destroyed the global integrity of the solution. In contrast, the CMoC solution remained well behaved throughout the calculation.

The lesson from Figures 20 and 21 is clear. The MoC has a general tendency to equilibrate the kinetic and magnetic energy densities (by erroneously increasing the Alfvén velocity at the expense of the flow velocity for weak magnetic fields and presumably the reverse for dominant magnetic fields) at accelerated rates. The most spectacular manifestations of this tendency are the magnetic "explosions" in which kinetic energy density in shear layers is incorrectly converted to magnetic energy density and subsequently transported into the rest of the solution. However, one does not need the explosions per se to do this. The tendency of the MoC to exaggerate the growth of magnetic energy density is insidious and has been observed by the author to affect simulations in which no actual explosions were seen. While the effect may be minor in most cases, it is well to conclude this section with the cautionary note that growth rates of magnetic field energy densities as computed by the MoC should be carefully scrutinized.

5. DISCUSSION AND A PREVIEW

This paper describes a new algorithmic approach for solving the time-dependent MHD equations numerically in multidimensions using methods of operator-splitting. This technique is characterized by resolving the three-dimensional cross product and curl (e.g., eq. [4] and the Lorentz force term in eq. [2]) into three independent planes (whence "planar-split") rather than into three independent directions (whence "directional-split"), as has been traditional. Thus, for example, within the (1, 2)-plane (normal in the 3-direction), v_1 and B_1 are interpolated in the 2-direction, and v_2 and B_2 are interpolated in the 1-direction all simultaneously and all to the same zone edges. Since these interpolations are upwinded in the characteristic velocities, which, in turn, are determined from the interpolated values, planar-split interpolations are performed implicitly. Continuing with the example, the interpolated values of v_1, v_2, B_1, and B_2 are then used to (1) transport s_2 in the 1-direction and s_1 in the 2-direction; (2) Lorentz-accelerate v_2 in the 1-direction and v_1 in the 2-direction; and (3) construct ϵ_3 (the 3-*emf*), used to update the magnetic fields. Planar-splitting acknowledges that the fundamental "building blocks" of the cross product in three dimensions are contained within the three orthogonal *planes* and not the three orthogonal *directions*. For example, the 3-component of $\boldsymbol{v} \times \boldsymbol{B}$ is given by $\epsilon_3 = v_1 B_2 - v_2 B_1$ and requires examination of the entire (1, 2)-plane (containing the 1- and 2-components of $\boldsymbol{v}$ and $\boldsymbol{B}$) rather than any one direction. In addition, transverse transport of momentum turns out to be performed more effectively in a planar-split scheme than in a directional-split one. Conversely, the fundamental building blocks of the divergence operator in three-dimensions are the three orthogonal directions, and, thus, transport of scalars and momenta longitudinal to the transport direction are treated effectively by the more traditional directional-splitting methods.

Despite (or perhaps because of) its algorithmic complexity, CMoC does not specifically address the issue of monotonicity in the magnetic field distribution. Loosely speaking, monotonicity is the requirement that no structures with scale sizes less than a few zones be allowed to develop or persist on the grid. For volume-conservative equations (eqs. [1], [2], and [3]), this is accomplished by exploiting a remarkable property of the differenced divergence operator: if the interpolations themselves are monotonic, the divergence operator will pass this property on to the updated flow variables.

Obviously, the induction equation (4) behaves very differently than the volume-conservative equations (1), (2), and (3). In particular, the original monotonic nature of the interpolations of $\boldsymbol{v}$ and $\boldsymbol{B}$ to the bases of the characteristics is *not* passed on to the updated magnetic field variables. Specifically, while the original interpolations of $\boldsymbol{v}$ and $\boldsymbol{B}$ are monotonic, the "starred" values (§§ 3.2, and 3.3) are not, as exemplified by the occasional "virtual exchange" of energy between the flow and Alfvén velocity fields (e.g., discussion following eq. [71]). Indeed, it is not clear what is meant by monotonicity in magnetic field structures, or even if this is a desired property. Unlike volume-conservative equations, some local extrema (defined by three zones) in the magnetic field *are* physically significant. For example, consider a shear layer in the (1, 2)-plane in which $\boldsymbol{v} = +v\boldsymbol{i}$ $(x_2 < 0)$, $\boldsymbol{v} = -v\boldsymbol{i}$ $(x_2 > 0)$, and an initial (dynamically weak) magnetic field given by $\boldsymbol{B} = +B\boldsymbol{j}$ permeates all space. After a single time step, this system will develop a 1-component of the magnetic field at $x_2 = 0$ *only*, right at the shear boundary. Everywhere else, B_1 will still be zero. In a strictly monotonic scheme, such a three-zone structure would be discouraged but clearly this is a critical first step for the shear layer to alter the direction of the magnetic field.[4]

Clearly, a mechanism to distinguish between desirable and undesirable deviations from monotonicity in the magnetic field distribution is required. Currently, no satisfactory discriminant has been developed, although a few possibilities exist. These may be generalized as follows. Instead of equation (4), consider the *resistive* induction equation, namely,

$$\frac{\partial \boldsymbol{B}}{\partial t} = \nabla \times (\boldsymbol{v} \times \boldsymbol{B} - \boldsymbol{E}) , \tag{92}$$

where, formally,

$$\boldsymbol{E} = \mathscr{R} \cdot \boldsymbol{J} = \mathscr{R} \cdot (\nabla \times \boldsymbol{B}) , \tag{93}$$

and where $\mathscr{R}$ is the resistivity tensor of the fluid. In the ideal MHD limit, $\mathscr{R} = 0$. Numerically, one is free to choose whatever $\boldsymbol{E}$ one likes, so long as it preserves the various CMoC criteria. In particular, one may set $\boldsymbol{E}$ to whatever is required to eliminate nonmonotonic behavior from the magnetic field profiles. In practice, this still necessitates determining which nonmonotonic behavior is desired and which is not.

Another approach is to define an artificial resistivity in analogy with the artificial viscosity (Appendix A):

$$\mathscr{R}_{aa} = \frac{Q_R J_a (\delta x_a)^2}{\sqrt{\rho}} , \qquad a = 1, 2, 3 , \tag{94}$$

with off-diagonal elements being zero. Q_R is a scaling parameter of order unity used to adjust the level of applied artificial resistivity, J_a is the a-component of the current density, δx_a is the length of a zone in the a-direction, and ρ is the density. Equation (94) is then used as the resistivity in equation (93) and, indirectly, equation (92), thus modifying the magnetic field.

Unfortunately, this manner of artificial resistivity can generate unacceptable levels of diffusion in the magnetic field distribution, even for small values of Q_R (J. Hawley & J. Stone 1993, private communication). This is not the case for artificial viscous heating across a shock front, since shocks are self-steepening (Appendix A). Thus, in practice, an equilibrium between the diffusive nature of artificial viscosity and the steepening nature of the shock is established, resulting in a rather constant shock width of 3 or 4 zones for operator-split schemes such as CMoC. However, artificial resistivity is applied across current sheets which are not self-steepening, and thus, current sheets tend to be diffused into oblivion. It may be that the form for $\mathscr{R}_{aa}$ in equation (94) is inappropriate. The problems of magnetic monotonicity in general, and of artificial resistivity in particular, are areas of current research and development.

Given the rather complex nature of the CMoC algorithm, an additional potential area for concern is efficiency. In fact, it turns out that the author's implementation of the CMoC and the MoC are comparable in speed. This is because the additional time required by CMoC to evaluate the characteristic speeds implicitly is roughly compensated for by the elimination of the Lagrangian MoC step for the transverse Lorentz forces and the MUTCI computations for the transverse transport of momentum. In practice, on a single C-90 processor, the CMoC can update as many as 330,000 one-dimensional mesh points, 210,000 two-dimensional mesh points, or 140,000 three-dimensional mesh points per second. On a Sparc 10, these numbers are 7500, 4500, and 3000, respectively. The CMoC is also manifestly parallelizable and can make efficient use of multiprocessor machines.

Finally, an example of a full-scale three-dimensional CMoC simulation is presented. Further details of this and other calculations will appear in the literature as the manuscripts are prepared. The "test" calculation in § 4.3 was performed at twice the resolution (7 million zones, 20 zones across the jet diameter) and run until the apex of the leading bow shock approached the outer boundary of the computational domain. The computer program used to generate these data, which embodies the CMoC algorithm, is called ZEUS-3D, a code related to, yet distinct from, a code by the same name currently being developed by M. Norman and collaborators at the University of Illinois.

Figure 22 shows two renderings of the final epoch of this jet. Figure 22*a* shows a two-dimensional slice of the density on a plane which includes the jet axis and exhibits the main features of the simulation (cf. Fig. 19). Figure 22*b* shows a line-of-sight integration

[4] Example attributed to J. Hawley (1992, private communication).

of the synchrotron emissivity (Stokes *I*), determined from the computed magnetic field, pressure, and density distributions. The interested reader might want to compare the Stokes *I* image in a generic sense with Figures 1 and 2 in Clarke et al. (1992). Notably absent in Figure 22*b* is a well-defined jet which is probably enhanced in nature by Doppler favoritism (not accounted for in the simulation). There is a "hot spot" at the tip of the jet in Figure 22*b*, though it is not the brightest feature on the image. Bright hot spots are probably sustainable only with much higher Mach numbers.

Perhaps the most impressive aspect of Figure 22*b* is the propensity of total intensity filaments in the "lobe" (labeled "shocked jet material" in Fig. 19) which, in the simulation, result from shear amplification of a weak magnetic field on dynamical timescales. These features are encouraged by the existence of large-scale shear layers (on the surfaces of giant eddies, for example) and discouraged by the cascade of the flow into turbulence. The balance of these two processes results in a pseudo–steady state situation in which filaments, whose widths are related to the thicknesses of the shear layers and whose lengths are related to the diameters of the eddies, are always present in the extended emission of the simulated radio lobe (Clarke 1993).

The spontaneous appearance of filaments in the simulation has immediate astrophysical applications. Total intensity filaments are a ubiquitous property of well-resolved extragalactic radio sources and, as such, require a simple, universal explanation. Until simulations such as this were performed, no such explanation was forthcoming (see, for example, Hines, Owen, & Eilek 1989). This result will be discusseed in more detail in a future paper.

Currently, the CMoC (as embodied by ZEUS-3D) is being used to expand the investigation of magnetized extragalactic radio jets. Determining whether magnetic fields in extragalactic radio sources are dynamically important is relevant both to observers who wish to understand the observed morphologies, and to theorists who ponder the origin of the magnetic field pervading the universe. Specifically, it is clear that the magnetic field plays an important role in the stability and morphology of an extragalactic radio source, and it may be possible to estimate the relative contribution of the magnetic field to the dynamics of a radio jet by carefully observing its morphological properties. Even if the magnetic field is of no dynamical consequence, its role in determining the apparent synchrotron appearance makes it a critical ingredient to any full-scale simulation. Thus, the development of an MHD algorithm such as the CMoC, capable of evolving the induction equation reliably for all fields strengths, is important to any study in which the evolution of the magnetic field plays a significant role.

The author is grateful for helpful discussions with J. Hawley and J. Stone, and for timely and helpful comments from the referee. Much of this work was performed at the Harvard-Smithsonian Center for Astrophysics and supported, in part, by NASA grant NAG 5-2077 to the author while at the Center for Astrophysics, and by NSF grant AST 9148279 to R. Narayan at Harvard University. Current support from the Natural Sciences and Engineering Research Council of Canada is gratefully acknowledged. Some of this work utilized the Cray 2 and Cray Y/MP systems, formerly at the National Center for Supercomputing Application, and the Cray C-90, currently at the Pittsburgh Supercomputer Center (through NSF grant AST 940010P).

APPENDIX A

SUB-CYCLED ARTIFICIAL VISCOSITY

Maintaining a sharp discontinuity in the fluid variables (e.g., shocks and contact discontinuities) is perhaps the most severe challenge to a general fluid solver. The operator-split upwinded scheme described in this paper uses an artificial viscosity based upon the scheme proposed by von Neumann & Richtmyer (1950) to track shocks accurately and stably. The von Neumann–Richtmyer scheme guarantees that both the entropy jump across a shock and the shock speed will be correct for a one-dimensional shock. As outlined below, this scheme has been extended in a rather ad hoc (although in an obvious) fashion to three dimensions.

A1. IMPLEMENTATION

Addition of artificial viscosity requires that equations (2) and (3) be modified as follows:

$$\frac{\partial \boldsymbol{s}}{\partial t} + \nabla \cdot (\boldsymbol{s}\boldsymbol{v}) = -\nabla p + (\nabla \times \boldsymbol{B}) \times \boldsymbol{B} - \nabla \cdot \mathcal{Q} , \tag{95}$$

$$\frac{\partial e}{\partial t} + \nabla \cdot (e\boldsymbol{v}) = -p\nabla \cdot \boldsymbol{v} - \mathcal{Q} : \nabla \boldsymbol{v} , \tag{96}$$

where $\mathcal{Q}$ is the artificial viscous stress tensor. In practice, the viscous terms are treated as ordinary source terms and are accounted for during the source step (§ 2.2). Specifically, the viscous source terms are applied to the velocities and internal energy after equation (19) (i.e., after velocities have been accelerated by the pressure gradients) and before equation (20) (i.e., before the $p\,dV$ cooling/heating of the internal energy density). In the von Neumann–Richtmyer scheme, one writes $\mathcal{Q}$ as a diagonal tensor. Thus, the viscous source terms are written as

$$\frac{\partial v_a}{\partial t} = -\frac{1}{\rho}\frac{\partial \mathcal{Q}_{aa}}{\partial x_a} , \qquad a = 1, 2, 3 , \tag{97}$$

$$\frac{\partial e}{\partial t} = -\sum_{a=1}^{3} \mathcal{Q}_{aa}\frac{\partial v_a}{\partial x_a} , \tag{98}$$

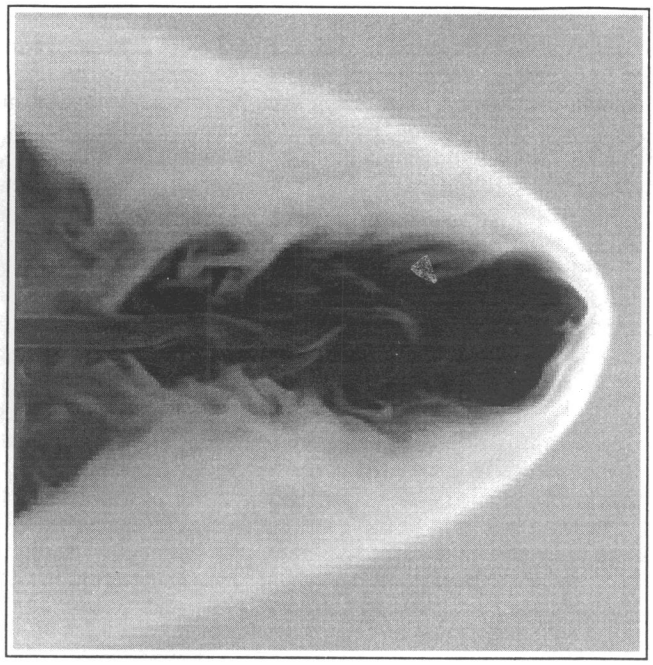

FIG. 22*a*

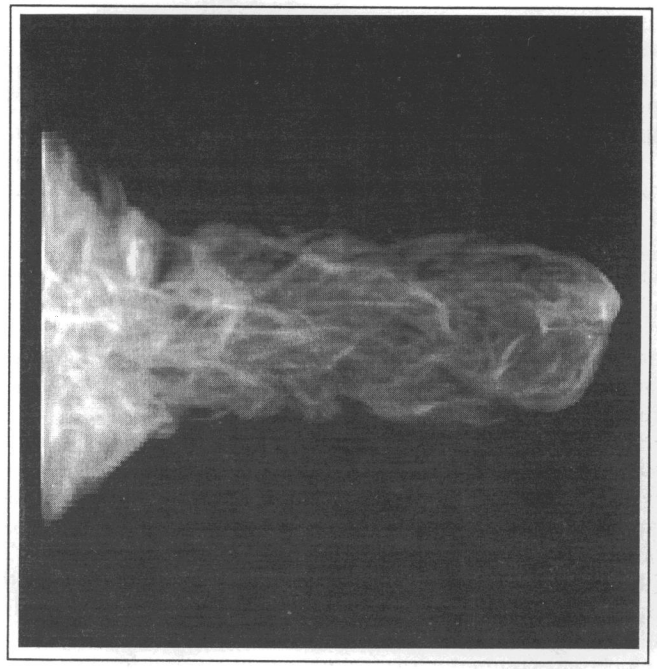

FIG. 22*b*

FIG. 22.—Two renderings of a three-dimensional simulation of an extragalactic radio jet computed by the CMoC algorithm and described in the text. (*a*) Density: This two-dimensional slice through the data cube along the jet axis shows the density ranging from 10^{-3} (*black*) to 3 (*white*) times the quiescent ambient density. The jet is clearly visible, as are the leading bow shock and the contact discontinuity separating the shocked jet and ambient media. Note the well-developed Kelvin-Helmholtz and Rayleigh-Taylor instabilities along the contact discontinuity. (*b*) Line-of-sight integration of synchrotron emissivity: The dynamic range of this image is ~ 1000. A logarithmic scale is used to emphasize the dimmer regions. Note the development of filaments in the extended regions of the lobe produced by the jet.

where $\mathcal{Q}_{aa}$ are the diagonal elements of the viscous stress tensor. Differencing equations (97) and (98), one gets

$$v_1^{n,S,S_{\mathcal{Q}}}(i,j,k) = v_1^{n,S}(i,j,k) - dt^n \frac{2}{d^n(i-1,j,k) + d^n(i,j,k)} \frac{\mathcal{Q}_{11}(i) - \mathcal{Q}_{11}(i-1)}{dx_{1b}(i)}, \tag{99}$$

$$v_2^{n,S,S_{\mathcal{Q}}}(i,j,k) = v_2^{n,S}(i,j,k) - dt^n \frac{2}{d^n(i,j-1,k) + d^n(i,j,k)} \frac{\mathcal{Q}_{22}(j) - \mathcal{Q}_{22}(j-1)}{dx_{2b}(j)}, \tag{100}$$

$$v_3^{n,S,S_{\mathcal{Q}}}(i,j,k) = v_3^{n,S}(i,j,k) - dt^n \frac{2}{d^n(i,j,k-1) + d^n(i,j,k)} \frac{\mathcal{Q}_{33}(k) - \mathcal{Q}_{33}(k-1)}{dx_{3b}(k)}, \tag{101}$$

$$e^{n,S_{\mathcal{Q}}}(i,j,k) = e^n(i,j,k) - dt^n \left[\mathcal{Q}_{11}(i) \frac{dv_1(i,j,k)}{dx_{1a}(i)} + \mathcal{Q}_{22}(j) \frac{dv_2(i,j,k)}{dx_{2a}(j)} + \mathcal{Q}_{33}(k) \frac{dv_3(i,j,k)}{dx_{3a}(k)} \right], \tag{102}$$

where the superscript S_Q indicates the variable has been updated with the artificial viscous source term and where

$$dv_1(i,j,k) \equiv v_1^{n,S}(i+1,j,k) - v_1^{n,S}(i,j,k), \tag{103}$$

$$dv_2(i,j,k) \equiv v_2^{n,S}(i,j+1,k) - v_2^{n,S}(i,j,k), \tag{104}$$

$$dv_3(i,j,k) \equiv v_3^{n,S}(i,j,k+1) - v_3^{n,S}(i,j,k). \tag{105}$$

Evidently, $\mathcal{Q}_{aa}$ are zone-centered quantities. While in principle one is free to choose any form for $\mathcal{Q}_{aa}$, a form which generates the correct entropy jump across a shock, yields the correct shock propagation velocity, *and* has negligibly small effects well away from shocks is the following:

$$\mathcal{Q}_{aa}(i) = d^n(i,j,k)\, dv_a(i,j,k)\{-Q_1\, c(i,j,k) + Q_2\ \mathrm{MAX}\ [0, dv_a(i,j,k)]\}, \tag{106}$$

where $c(i,j,k)$ is the sound speed given by equation (14). The first term (proportional to the free parameter Q_1) is the *linear viscosity* and has been found to be useful in stabilizing the flow after extremely strong shocks or in stagnant regions. When needed, Q_1 is typically set to 0.1–0.4. For most applications, however, Q_1 is set to zero. The second term (proportional to the free parameter Q_2) is the *quadratic viscosity* and corresponds to the original form given by von Neumann & Richtmyer (1950). The parameter Q_2 may be interpreted roughly as one or two less than the number of zones over which a shock (which, in principle, should be contained within a single zone) is "smeared out" by the artificial viscosity. Thus, for a typical setting of $Q_2 = 2$, shocks are captured within three or four zones. It is the act of smearing out the shock over a finite number of zones which renders the algorithm stable to the formation

of such discontinuities. Since shocks are self-steepening phenomena, a balance is struck between the self-steepening nature of the shock and the diffusive nature of the artificial viscosity. Thus, shock widths are relatively constant—they do not continue to smear out indefinitely as a contact discontinuity might under the influence of diffusion, or a current sheet might under the influence of resistivity. Finally, the "MAX" function ensures that quadratic viscosity will be applied only to compressional regions (e.g., shocks) and not expanding regions where artificial viscosity is not required.

Strictly speaking, the three-dimensional extension of the von Neumann–Richtmyer scheme discussed above is valid only for Cartesian geometry. A tensor treatment of the artificial viscosity which may be more suitable for general curvilinear coordinates is discussed in SNa.

A2. TIME-STEP CONSIDERATIONS

The Navier-Stokes equation differs from equation (2) by the addition of the term

$$\frac{\partial \boldsymbol{v}}{\partial t} = \nu \nabla^2 \boldsymbol{v} , \tag{107}$$

where ν is the kinematic viscosity. Consider the 1-component of this equation with symmetry in the 2- and 3-directions:

$$\frac{\partial v_1}{\partial t} = \nu \frac{\partial^2 v_1}{\partial x_1^2} . \tag{108}$$

Now, for comparison, substitute equation (106) (with $a = 1$, assuming $Q_1 = 0$ and $dv_1 < 0$) in equation (97) and rearrange (assuming ρ = constant for simplicity) to get

$$\frac{\partial v_1}{\partial t} = -2Q_2\, dv_1\, dx_1 \frac{\partial^2 v_1}{\partial x_1^2} , \tag{109}$$

Thus, artificial viscosity is formally equivalent to viscous diffusion with an effective kinematic viscosity given by

$$\nu_{2_{11}} = -2Q_2\, dv_1\, dx_1 = 2Q_2 |dv_1|\, dx_1 \tag{110}$$

For stability, explicit diffusion operators are limited to the diffusion time step given by (e.g., Richtmyer & Morton 1967)

$$dt \le \frac{(dx)^2}{2\nu} . \tag{111}$$

Thus, by analogy, the artificial viscosity also places restrictions on the time step, namely,

$$dt_{2_{11}} \le \frac{(dx_1)^2}{2\nu_{2_{11}}} = \frac{dx_1}{4Q_2 |dv_1|} . \tag{112}$$

Therefore, for the three-dimensional extension to the von Neumann–Richtmyer scheme discussed above, the time step must be less than

$$dt_2 = \underset{\forall i,j,k}{\mathrm{MIN}} \left[\frac{dx_1(i)}{4Q_2 |dv_1(i,j,k)|} , \frac{dx_2(j)}{4Q_2 |dv_2(i,j,k)|} , \frac{dx_3(k)}{4Q_2 |dv_3(i,j,k)|} \right] . \tag{113}$$

In principle, the final time step used to advance the explicit scheme should be the *lesser* of dt_2 (as determined by eq. [113]) and dt^n (as determined by eq. [13]). Unfortunately, equation (113) can place severe restrictions on the rate at which the solution converges. Indeed, for any system in which strong shocks play a role, the viscous time step will dominate the dynamics. To see this, note that if strong shocks are likely to occur, this means the flow speed will dominate the CFL limit as given by equation (13). Thus, $dt^n \sim dx/v$. Now at a strong shock, $dv \sim v$ (velocities strongly decelerated), and, thus, from equation (113), $dt_2 \sim dx/4Q_2 v$, a factor of 8 *less* than dt^n for the typical value $Q_2 = 2$. This can be an intolerable price to pay since it eliminates one of the major advantages of an operator-split upwinded scheme over Godunov-type schemes such as PPM, namely, computational speed. With the artificial viscosity dominating the CFL limit, such a scheme could take several times as many time steps as PPM would on the same problem.

To circumvent this problem, one notes that the viscous step is entirely confined to the source step, and thus one may "subcycle" on the artificial viscosity. Thus, the MHD cycle as described in the main text (including all nonviscous source terms, transport, and induction) is performed using the time step given by equation (13). However, the viscous stresses and heating are computed on the (typically shorter) viscous time step given by equation (113). Thus, dt_2 should replace dt^n in equations (99)–(102). A sufficient number of viscous steps are taken so the problem time accumulated on the viscous timescale is equal to the dynamical time step used for the rest of the cycle.

Of course, subcycling on the artificial viscosity does not, in general, give identical results to those obtained by computing the entire problem on the viscous time step. The truncation errors introduced by subcycling can be reduced, however, if the viscous stresses and heating are time-centered. This can be accomplished by making two passes through the viscous routine for every viscous subcycle. The first pass is performed at half the viscous time step and generates partially accelerated velocities retained as separate quantities. The second pass then updates the original velocities and the internal energy density with the viscous source terms, using the full viscous time step and the partially accelerated velocities from the first pass to determine the velocity divergences

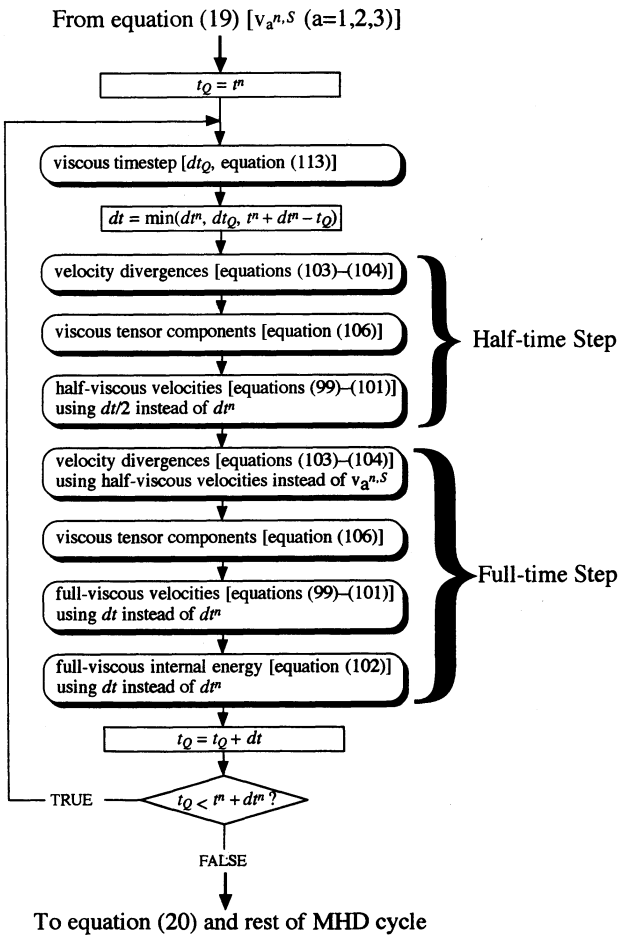

FIG. 23.—Detailed flowchart of the subcycled artificial viscosity algorithm as implemented in the ZEUS-3D computer program

(eqs. [103], [104], and [105]). By time-centering the viscous update in this way, detailed agreement between the solutions with and without subcycling is greatly improved.

Figure 23 is a detailed flowchart showing how the subcycled artificial viscosity has been implemented in ZEUS-3D.

APPENDIX B

TOTAL ENERGY EQUATION

One possible variation on the algorithm presented herein is to replace equation (3) with the total energy equation. Defining the total energy E as

$$E \equiv e + \frac{1}{2}\rho v^2 + \frac{B^2}{2}, \tag{114}$$

where $v = |\boldsymbol{v}|$ and $B = |\boldsymbol{B}|$, the time derivative of E may be evaluated from equations (1)–(4) to get

$$\frac{\partial E}{\partial t} + \nabla \cdot \boldsymbol{v}(E + p^*) + \nabla \cdot \boldsymbol{q} - \nabla \cdot \boldsymbol{B}(\boldsymbol{v} \cdot \boldsymbol{B}) = \boldsymbol{v} \cdot \nabla(B^2) - 2\boldsymbol{B} \cdot [(\boldsymbol{v} \cdot \nabla)\boldsymbol{B}], \tag{115}$$

where $p^* \equiv p + B^2/2$; $\boldsymbol{q} = (v_1 \mathcal{Q}_{11}, v_2 \mathcal{Q}_{22}, v_3 \mathcal{Q}_{33})$, $\mathcal{Q}_{aa}$, $a = 1, 2, 3$, are the von Neumann–Richtmyer artificial viscous stresses defined in Appendix A (eq. [106]); and where the right-hand side of equation (115) is identically zero for Cartesian, cylindrical, spherical polar, and other suitably behaved coordinate systems. Note that equations (114) and (115) can be extended trivially to include the gravitational potential, if desired.

Equation (115) is then cast into integral form to get

$$\frac{d}{dt}\int_V E\, dV + \oint_A [(E + p^*)\boldsymbol{v} + \boldsymbol{q} - (\boldsymbol{v} \cdot \boldsymbol{B})\boldsymbol{B}] \cdot d\boldsymbol{A} = 0. \tag{116}$$

As there are no longer any sources (right-hand side = 0), the update of E may be performed by three transport steps, namely, T_1, T_2, and T_3. Thus, considering transport in the 1-direction only, equation (116) becomes

$$\left.\frac{d}{dt}\int_V E\,dV\right|_1 = -\oint_{A_1} Ev_1\,dA_1 - \oint_{A_1}(p^* + \mathcal{Q}_{11})v_1\,dA_1 + \oint_{A_1}(\boldsymbol{v}\cdot\boldsymbol{B})B_1\,dA_1\,. \tag{117}$$

Differencing equation (117) gives

$$E^{n,T_1}(i,j,k) = E^n(i,j,k) - \frac{\mathcal{F}_1(i+1,j,k)-\mathcal{F}_1(i,j,k)}{dx_{1a}(i)} - \frac{\mathcal{G}_1(i+1,j,k)-\mathcal{G}_1(i,j,k)}{dx_{1a}(i)} + \frac{\mathcal{H}_1(i+1,j,k)-\mathcal{H}_1(i,j,k)}{dx_{1a}(i)}\,, \tag{118}$$

where $\mathcal{F}_1(i,j,k)$ and $\mathcal{G}_1(i,j,k)$ are the fluxes of total energy (E) and total pressure ($P \equiv p^* + \mathcal{Q}_{11}$), respectively, across the i-face and are given by

$$\mathcal{F}_1(i,j,k) \equiv \mathcal{M}_1(i,j,k)\overline{[E^n(i,j,k)/d^n(i,j,k)]}^{i}\,, \tag{119}$$

$$\mathcal{G}_1(i,j,k) \equiv \mathcal{M}_1(i,j,k)\overline{P^n(i,j,k)/d^n(i,j,k)]}^{i}\,. \tag{120}$$

The mass flux $\mathcal{M}_1(i,j,k)$ is given by equation (24), and $P^n(i,j,k)$ is given by

$$\begin{aligned} P^n(i,j,k) = E^n(i,j,k) + \mathcal{Q}_{11} - \tfrac{1}{8}d^n(i,j,k)\{&[v_1^n(i,j,k) + v_1^n(i+1,j,k)]^2 \\ &+ [v_2^n(i,j,k) + v_2^n(i,j+1,k)]^2 + [v_3^n(i,j,k) + v_3^n(i,j,k+1)]^2\} \end{aligned} \tag{121}$$

where $\mathcal{Q}_{11}$ is given by equation (106). The separation of the total energy and total pressure fluxes is deliberate. Thus, two separate interpolations (specific energy and "specific pressure") are required. If, instead, the total energy and total pressure are combined and their sum interpolated, monotonicity of E is no longer ensured and the algorithm becomes unstable.

In the last term of equation (118), $\mathcal{H}_1$ is not a true flux since "transport" is performed by B_1 not v_1. There are a variety of ways to define $\mathcal{H}_1$, and one that works reasonably well is

$$\mathcal{H}_1(i,j,k) \equiv [v_1^n(i,j,k)B_1^n(i,j,k) + \langle v_2^n\rangle_{2,1}\langle B_2^n\rangle_{2,1} + \langle v_3^n\rangle_{3,1}\langle B_3^n\rangle_{3,1}]B_1^n(i,j,k)\,dt^n\,, \tag{122}$$

where the angle brackets indicate a four-point average of the enclosed quantity necessary to estimate the quantity at the i-face. Thus, for example,

$$\langle v_2^n\rangle_{2,1} \equiv \tfrac{1}{4}[v_2^n(i,j,k) + v_2^n(i,j+1,k) + v_2^n(i-1,j,k) + v_2^n(i-1,j+1,k)]\,. \tag{123}$$

Notice that no averaging is necessary for the $v_1^nB_1^n$ term, since it is already located at the i-face.

By permuting the labels and indices, difference expressions for the transport of E in the 2- and 3-directions are given by

$$E^{n,T_1,T_2}(i,j,k) = E^{n,T_1}(i,j,k) - \frac{\mathcal{F}_2(i,j+1,k)-\mathcal{F}_2(i,j,k)}{dx_{2a}(j)} - \frac{\mathcal{G}_2(i,j+1,k)-\mathcal{G}_2(i,j,k)}{dx_{2a}(j)} + \frac{\mathcal{H}_2(i,j+1,k)-\mathcal{H}_2(i,j,k)}{dx_{2a}(j)}\,, \tag{124}$$

$$\begin{aligned} E^{n,T_1,T_2,T_3}(i,j,k) &\equiv E^{n+1}(i,j,k) \\ &= E^{n,T_1,T_2}(i,j,k) - \frac{\mathcal{F}_3(i,j,k+1)-\mathcal{F}_3(i,j,k)}{dx_{3a}(k)} - \frac{\mathcal{G}_3(i,j,k+1)-\mathcal{G}_3(i,j,k)}{dx_{3a}(k)} + \frac{\mathcal{H}_3(i,j,k+1)-\mathcal{H}_3(i,j,k)}{dx_{3a}(k)}\,, \end{aligned} \tag{125}$$

where

$$\mathcal{F}_2(i,j,k) \equiv \mathcal{M}_2(i,j,k)\overline{[E^{n,T_1}(i,j,k)/d^{n,T_1}(i,j,k)]}^{j}\,, \tag{126}$$

$$\mathcal{G}_2(i,j,k) \equiv \mathcal{M}_2(i,j,k)\overline{[P^{n,T_1}(i,j,k)/d^{n,T_1}(i,j,k)]}^{j}\,, \tag{127}$$

$$\mathcal{H}_2(i,j,k) \equiv [v_2^n(i,j,k)B_2^n(i,j,k) + \langle v_3^n\rangle_{3,2}\langle B_3^n\rangle_{3,2} + \langle v_1^n\rangle_{1,2}\langle B_1^n\rangle_{1,2}]B_2^n(i,j,k)\,dt^n\,, \tag{128}$$

$$\mathcal{F}_3(i,j,k) \equiv \mathcal{M}_3(i,j,k)\overline{[E^{n,T_1,T_2}(i,j,k)/d^{n,T_1,T_2}(i,j,k)]}^{k}\,, \tag{129}$$

$$\mathcal{G}_3(i,j,k) \equiv \mathcal{M}_3(i,j,k)\overline{[P^{n,T_1,T_2}(i,j,k)/d^{n,T_1,T_2}(i,j,k)]}^{k}\,, \tag{130}$$

$$\mathcal{H}_3(i,j,k) \equiv [v_3^n(i,j,k)B_3^n(i,j,k) + \langle v_1^n\rangle_{1,3}\langle B_1^n\rangle_{1,3} + \langle v_2^n\rangle_{2,3}\langle B_2^n\rangle_{2,3}]B_3^n(i,j,k)\,dt^n\,. \tag{131}$$

Note that the artificial viscosity is now an integral part of the transport step. No separate viscous source term should be applied to the internal energy density, and equation (102) is skipped. Unfortunately, because the artificial viscosity is no longer isolated in a single module (as is the case when the internal energy equation is solved), subcycling on the viscous time step can no longer be performed (Appendix A). Thus, the CFL limit now requires the time step be set to the *lesser* of the time steps evaluated by equations (13) and (113).

Solving the total energy equation rather than the internal energy equation has the advantage of ensuring total energy conservation to within machine round-off error. For some applications (e.g., strong shocks), this may be a critical consideration. However, in practice, because the thermal pressure is now the difference between two numerically determined quantities (E and $\rho v^2/2$), numerical noise can be amplified and generate negative pressures, especially in highly supersonic flow. This can lead to problems much worse than violation of strict energy conservation. In addition, not subcycling on the viscous time step can decrease computational

efficiency dramatically (Appendix A). Thus, unless strict total energy conservation is of paramount importance (e.g., the second test problem in § 4.1), and where computational speed is an important consideration, calculations should be performed by solving the internal energy equation.

REFERENCES

Balbus, S. A., & Hawley, J. F. 1992, ApJ, 400, 610
Beck, R., & Kronberg, P. 1990, in IAU Symp. 140, Galactic and Intergalactic Magnetic Fields, ed. R. Beck & P. Kronberg (Dordrecht: Reidel)
Bell, J. B., Colella, P., & Trangenstein, J. A. 1989, J. Comp. Phys., 82, 362
Boris, J. P., & Book, D. L. 1973, J. Comp. Phys., 11, 38
Brio, M., & Wu, C. C. 1988, J. Comp. Phys., 75, 400
Clarke, D. A. 1993, in Jets in Extragalactic Radio Sources (Proc. of the Second Ringberg Castle Workshop), ed. H.-J. Röser & K. Meisenheimer (Berlin: Springer), 243
Clarke, D. A., Bridle, A. H., Burns, J. O., Perley, R. A., & Norman, M. L. 1992, ApJ, 385, 173
Clarke, D. A., Norman, M. L., & Burns, J. O. 1989, ApJ, 342, 200
Colella, P., & Woodward, P. R. 1984, J. Comp. Phys., 54, 174
Courant, R., Friedrichs, K. O., & Lewy, H. 1928, Math. Ann., 100, 32
Dai, W., & Woodward, P. R. 1994, J. Comp. Phys., 111, 354
DeVore, C. R. 1991, J. Comp. Phys., 92, 142
Evans, C. R., & Hawley, J. F. 1988, ApJ, 332, 659 (EH)
Godunov, S. K. 1959, Mat. Sb., 47, 271
Harten, A. 1983, J. Comp. Phys., 49, 357
Harten, A., Engquist, B., Osher, S., & Chakravarthy, S. R. 1987, J. Comp. Phys., 71, 231
Hines, D. C., Owen, F. N., & Eilek, J. A. 1989, ApJ, 347, 713
Kronberg, P. P. 1994, Rep. Prog. Phys., 57, 325
Norman, M. L., Wilson, J.R., & Barton, R. 1980, ApJ, 239, 968
Norman, M. L., & Winkler, K.-H., A. 1986, in Astrophysical Radiation Hydrodynamics (Proc. of NATO Adv. Res. Workshop), ed. K.-H. A. Winkler & M. L. Norman (Munich: M. P. I. für Physik und Astrophysik), 187
Patnaik, G., Guirguis, R. H., Boris, J. P., & Oran, E. S. 1987, J. Comp. Phys., 71, 1
Richtmyer, R. D., & Morton, K. W. 1967, Difference Methods for Initial-Value Problems (2d ed.; New York: Wiley Interscience)
Roe, P. L. 1981, J. Comp. Phys., 43, 357
Ryu, D., & Jones, T. W. 1995, ApJ, 442, 228 (RJ)
Stone, J. M., Hawley, J. F., Evans, C. R., & Norman, M. L. 1992, ApJ, 388, 415
Stone, J. M., Mihalas, D., & Norman, M. L. 1992, ApJS, 80, 819
Stone, J. M., & Norman, M. L. 1992a, ApJS, 80, 753 (SNa)
———. 1992b, ApJS, 80, 791 (SNb)
van Leer, B. 1977, J. Comp. Phys., 23, 276
———. 1979, J. Comp. Phys., 32, 101
von Neumann, J., & Richtmyer, R. D. 1950, J. Appl. Phys., 21, 232
Zachary, A. L., & Colella, P. 1992, J. Comput. Phys., 99, 341